

# No Modality Left Behind: Adapting to Missing Modalities via Knowledge Distillation for Brain Tumor Segmentation

Shenghao Zhu<sup>a,\*</sup>, Yifei Chen<sup>b,\*</sup>, Weihong Chen<sup>a</sup>, Shuo Jiang<sup>a</sup>, Guanyu Zhou<sup>a</sup>, Yuanhan Wang<sup>a</sup>, Feiwei Qin<sup>a, \*\*</sup>, Changmiao Wang<sup>c</sup>, Qiyuan Tian<sup>b, \*\*</sup>

<sup>a</sup>*Hangzhou Dianzi University, Hangzhou, China*

<sup>b</sup>*Tsinghua University, Beijing, China*

<sup>c</sup>*Shenzhen Research Institute of Big Data, Shenzhen, China*

---

## Abstract

Accurate brain tumor segmentation is essential for preoperative evaluation and personalized treatment. Multi-modal MRI is widely used due to its ability to capture complementary tumor features across different sequences. However, in clinical practice, missing modalities are common, limiting the robustness and generalizability of existing deep learning methods that rely on complete inputs, especially under non-dominant modality combinations. To address this, we propose AdaMM, a multi-modal brain tumor segmentation framework tailored for missing-modality scenarios, centered on knowledge distillation and composed of three synergistic modules. The Graph-guided Adaptive Refinement Module explicitly models semantic associations between generalizable and modality-specific features, enhancing adaptability to modality absence. The Bi-Bottleneck Distillation Module transfers structural and textural knowledge from teacher to student models via global style matching and adversarial feature alignment. The Lesion-Presence-Guided Reliability Module predicts prior probabilities of lesion types through an auxiliary classification task, effectively suppressing false positives under incomplete inputs. Extensive experiments on the BraTS 2018 and 2024 datasets demonstrate that AdaMM consistently outperforms existing methods, exhibiting superior segmentation accuracy and robustness, particularly

---

<sup>\*</sup>These authors contributed equally to this work.

<sup>\*\*</sup>Corresponding authors: Feiwei Qin (qinfeiwei@hdu.edu.cn), Qiyuan Tian (qiyuan-tian@tsinghua.edu.cn).

in single-modality and weak-modality configurations. In addition, we conduct a systematic evaluation of six categories of missing-modality strategies, confirming the superiority of knowledge distillation and offering practical guidance for method selection and future research. Our source code is available at <https://github.com/Quanato607/AdaMM>.

*Keywords:* Multi-modal MRI, Missing Modality, Modality Adaptation, Knowledge Distillation, Graph Neural Network, Lesion-aware Segmentation

---

## 1. Introduction

With the increasing prevalence of brain tumors, precise segmentation from neuroimaging has become an essential prerequisite for effective diagnosis, individualized therapeutic strategies, and long-term outcome prediction [1]. Magnetic resonance imaging (MRI) offers high-resolution visualization of soft-tissue lesions and captures rich, complementary tumor characteristics across multiple imaging modalities. Specifically, T1-weighted imaging (T1) excels at delineating anatomical structures and vascular edema in subacute stroke, whereas T2-weighted imaging (T2) effectively depicts tissue edema and lesion boundaries [2]. Contrast-enhanced T1-weighted imaging (T1Gd) reveals intratumoral vasculature and blood-brain-barrier disruption via gadolinium enhancement, and fluid-attenuated inversion recovery (FLAIR) comprehensively visualizes abnormal signals associated with stroke and tumor infiltration [3]. These modalities not only reflect distinct pathological features but also exhibit varying sensitivity to tumor subregions such as the enhancing core, edema (ED), and necrotic areas. The information provided by these modalities is strongly complementary; their combined use furnishes critical evidence for accurate localization, morphological characterization, and fine-grained segmentation of brain tumors. Consequently, multi-modal MRI has become the method of choice for visual analysis and automated segmentation of brain tumors [4].

In recent years, advances in automated brain tumor segmentation algorithms have substantially reduced the manual effort required for delineation and improved segmentation accuracy [5, 6]. Nevertheless, MRI acquisition in clinical practice is often constrained, and only a subset of modalities is typically available. In contrast, most existing algorithms rely heavily on complete multimodal inputs and exhibit pronounced performance degradation when any modality is missing. Accordingly, a brain-tumor segmentation

approach that remains robust to modality absence and is tailored to diverse modality configurations is urgently needed. Traditional generic segmentation models, which lack dedicated modeling for specific modality combinations, frequently display notable instability across different subsets [7, 8]. For example, the T1Gd modality, which has a strong capability for Enhancing Tumor (ET) segmentation, achieves satisfactory results even under single-modality input, whereas the T1 and T2 modalities, which are relatively less effective for ET segmentation, perform poorly in their respective single-modality settings and still yield limited performance when jointly inferred [9, 10]. These observations indicate that generic models tend to optimize parameters for modalities with prominent segmentation cues, thus attaining superior performance on dominant modalities while failing to adapt to weaker combinations and consequently impairing overall performance. Hence, generic strategies are constrained under modality absence or non-dominant modality combinations, requiring more targeted, structurally adaptive mechanisms to enhance consistency and robustness in multi-modal settings.

To address this challenge, we propose an Adapter-based Missing Modality (AdaMM) Network comprising a Graph-guided Adaptive Refinement Module (GARM), a Bi-Bottleneck Distillation Module (BBDM), and a Lesion-Presence-Guided Reliability Module (LGRM). In GARM, a lightweight 3D residual module based on an Adapter Bank captures combination-specific features, while a graph convolutional network replaces conventional convolutions to address their weakness in modeling irregular and long-range dependencies, thereby enhancing semantic association modeling and representation refinement. In BBDM, a Global Style Matching Module (GSME) and a teacher-student discriminator, coupled with adversarial feature alignment and mean-squared-error loss, achieve precise matching and fusion of bottleneck features between teacher and student models, preserving structural information and textural details between missing-modality and complete-modality pathways and markedly improving robustness and accuracy under modality absence. In LGRM, a lightweight auxiliary classification branch predicts the presence probabilities of lesion types, providing priors for segmentation and distillation and effectively suppressing false positives in hollow regions under missing-modality conditions.

Meanwhile, during preliminary investigations of this study, we found that Zhou *et al.* [11] systematically categorized existing missing-modality learning methods as imputation-based or imputation-free. Imputation-based approaches compensate for missing modalities by generating data, creating fea-

tures, or retrieving samples. Data generation methods employ generative adversarial networks (GANs) [12] or variational autoencoders (VAEs) [13] to synthesize missing images conditioned on available modalities; however, the synthetic outputs often lack clinical realism and anatomical fidelity. Feature generation methods predict missing modality features via aggregation mechanisms but heavily depend on existing modalities and fail to recover critical diagnostic cues of the absent modality. Sample retrieval strategies select similar, fully modal cases to supplement missing information, but are limited by the quality of the database and entail high computational costs. Imputation-free methods eschew data synthesis and instead enhance performance through multi-task learning, knowledge distillation, or robustness-oriented strategies. Multi-task learning introduces auxiliary tasks to promote robust shared representations but requires careful weight balancing; knowledge distillation transfers knowledge via teacher-student architectures, boosting accuracy yet risking loss of deep semantic information and involving complex design; robustness enhancement leverages data augmentation or adversarial training to improve tolerance to modality absence, but its efficacy depends on meticulous strategy and parameter selection.

These insights motivated a comprehensive comparative study across the six methodological categories, analyzing brain-tumor segmentation under missing-modality scenarios. Accurate delineation of key tumor regions guides preoperative planning and radiotherapy dosage design, making high performance under modalities absent clinically critical. Experiments on the BraTS 2018 [14] and BraTS 2024 [15] datasets, widely regarded as gold standards, reveal pronounced differences, with knowledge-distillation methods demonstrating clear superiority. By transferring knowledge from complete-modality models, distillation effectively preserves crucial features and maintains high segmentation accuracy despite modality loss. Imputation-based methods can synthesize missing modalities, but the clinical relevance of the generated images remains challenging. In contrast, robustness enhancement and multi-task learning improve adaptability, yet still face limitations in complex missing-modality scenarios. These findings substantiate the advantage of knowledge distillation and provide new perspectives for future research.

The main contributions of this work are as follows:

1. We design the BBDM, integrating global style matching with adversarial alignment to achieve precise matching of teacher-student bottleneck features, markedly improving segmentation robustness and accuracy

under modality absence. This design ensures that both global structural patterns and fine-grained textural cues are faithfully preserved, even when critical modalities are missing.

2. We propose the GARM, which explicitly models semantic associations between generalizable and modality-specific features via a graph structure, enabling adaptive enhancement and refined fusion across modality combinations. By leveraging graph-based message passing, the module adaptively emphasizes informative modalities and compensates weaker ones, yielding more balanced and robust representations.
3. We introduce the LGRM, which guides segmentation by predicting prior probabilities of lesion presence, effectively reducing false segmentation under missing modalities and enhancing cross-modal consistency and reliability. The lesion-aware priors act as a soft constraint during inference, steering the network toward anatomically plausible predictions and improving diagnostic trustworthiness.
4. We conduct a comprehensive evaluation across six methodological categories for missing-modality brain tumor segmentation, encompassing over 15 representative models and 15 modality combinations. This large-scale study confirms the consistent superiority of knowledge distillation in maintaining segmentation accuracy under diverse and challenging scenarios, while offering a valuable reference for algorithm selection and future methodological development.

## 2. Related Work

### 2.1. *Imputation-Based Methods*

In multi-modal segmentation tasks, Imputation-Based methods explicitly complete missing features or data to recover comprehensive multi-modal semantics. By doing so, a model can maintain, or even substantially enhance, its performance when modalities are absent and can introduce new, more realistic samples into the dataset via generative models such as GANs [12] or VAEs [13]; certain feature-generation strategies adapt well to both homogeneous and heterogeneous data. Nevertheless, these approaches come at a cost: generative models are often complex to train and resource-intensive, and low-quality supplementary data may inject noise into the dataset. When training data are limited or model tuning is inadequate, the model readily

overfits the generated data, and the generative model itself may suffer mode collapse [16], diminishing its ability to faithfully capture the true distribution.

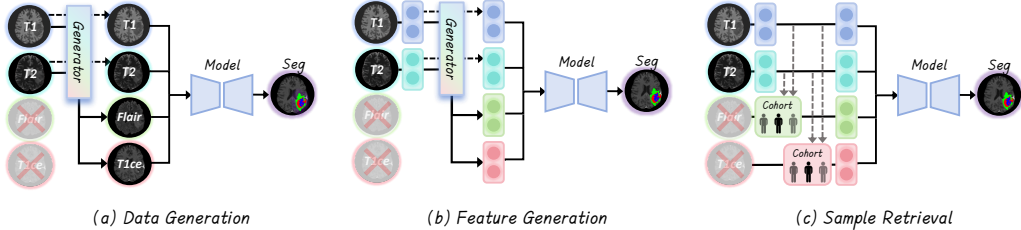


Figure 1: (a) **Data Generation**: an external generator synthesizes absent modalities, creating a full four-channel input for the segmentation model. (b) **Feature Generation**: the network learns to hallucinate modality-specific features internally when inputs are missing. (c) **Sample Retrieval**: the pipeline retrieves training cases from modality-matched cohorts to substitute for absent scans before segmentation.

### 2.1.1. Feature Generation

These methods first extract shared or contextual features from observed modalities, then synthesize representations in feature space that align with the semantics of the missing modality, and finally perform precise segmentation using the combined features. Representative examples include LCKD by Wang *et al.* [17], which automatically elects the most informative teacher modalities and distills their critical knowledge to student modalities, and ShaSpec proposed by Wang *et al.* [18], which supplements missing features through a shared-and-specific dual-branch extractor and a mean-extrapolation strategy. Ting *et al.* [19] further introduced the Multimodal Transformer of Incomplete MRI Data, which explicitly models cross-modal long-range dependencies via self-attention to reconstruct missing sequences at a highly fine granularity. These approaches reduce information loss without synthesizing images, yet they remain insufficiently robust to significant cross-domain distribution shifts and high-dimensional feature noise.

### 2.1.2. Data Generation

These methods employ generative models (e.g., GANs, VAEs) to first complete the missing modality and then feed the synthesized sequence into the segmentation network. Notable examples include MouseGAN++ by Yu *et al.* [20], which leverages a disentangling-contrastive GAN to preserve anatomical structure and contrast, enabling generation of multi-sequence

MRI from a single sequence; Hyper-GAE by Yang *et al.* [21], which uses a hyper-network and graph-attention mechanism to simultaneously complete all missing sequences in a shared space and optimizes end-to-end with the segmentation network; and SRMNet by Zhang *et al.* [22], which introduces deformation-aware reconstruction and key-information mining in the reconstruction branch, substantially enhancing segmentation robustness under complex missing-combination scenarios. Although these methods explicitly complete the inputs, they incur considerable training and inference overhead, and the clinical consistency of the generated modalities remains limited.

### 2.1.3. Sample Retrieval

Current sample-retrieval methods for handling missing modalities fall into three categories. The first retrieves samples from an external dataset by computing structural or semantic mask similarity (e.g., LRAA [23]), necessitating large data volumes; the second searches within the same batch using mask similarity (e.g., M3Care [24]), which inherently confines retrieval to in-batch samples and struggles with flexible missing-combination scenarios; the third aligns dual modalities of text and images for retrieval (e.g., SMCMSA [25]), which applies only to classification tasks and is limited to text–image alignment. All three exhibit notably weak robustness to missing modalities typically accommodating only one or two missing modalities and, given the diversity of tumor presentations, classification-oriented retrieval may introduce erroneous information. Consequently, these strategies are largely unsuitable for missing-modality brain-tumor segmentation.

## 2.2. Imputation-Free Methods

In contrast to explicit completion, Imputation-Free methods do not attempt to reconstruct missing modalities; instead, they perform inference directly on incomplete inputs, emphasizing generalization and robustness to any missing-modality combination. Eliminating generation or retrieval markedly reduces computational cost [26] and yields a lightweight inference pipeline, and avoids dependence on a specific completion module, thereby conferring high flexibility across datasets and applications. Robust losses and cooperative mechanisms tailored to missing modalities further endow the model with strong adaptability, enabling solid performance despite incomplete data [5]. However, because fine-grained information carried by unobserved modalities cannot be explicitly recovered, the depth of semantic characterization is limited and ultimately hinges on the quality and coverage

of the observed data [27], meaning that when information is scarce or noisy, results may be incomplete or imprecise.

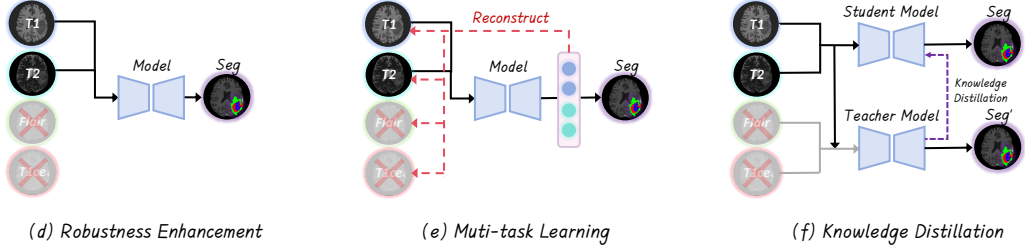


Figure 2: (d) **Robustness Enhancement**: the network is trained with random modality dropout so it can segment directly from whatever scans are available. (e) **Multi-task Learning**: an auxiliary decoder reconstructs the absent modalities (red dashed arrows) while the main branch outputs the segmentation mask. (f) **Knowledge Distillation**: a full-modality teacher guides a partial-modality student through feature and prediction alignment, boosting accuracy under incomplete inputs.

### 2.2.1. Robust Enhancement

These methods design robustness-oriented training strategies to strengthen model generalization and adaptability under missing modalities. Ding *et al.* [28] first proposed a Region-aware Fusion Network (RFNet) that adaptively aggregates multi-modal features by exploiting spatial relationships between modalities and tumor regions, significantly enhancing segmentation performance under incomplete modality scenarios. Zhang *et al.* [29] subsequently introduced mmFormer, which combines modality-specific encoders with a cross-modal Transformer to capture long-range inter-modal dependencies, enhancing adaptability to arbitrary modality loss. Most recently, Shi *et al.* [30] proposed M<sup>2</sup>FTrans, which incorporates a modality-masking fusion Transformer whose masked self-attention and modality-specific feature re-weighting effectively address different missing-modality scenarios. Although these methods improve robustness, they may still face performance bottlenecks under extreme absence.

### 2.2.2. Multi-Task Learning

These methods optimize multiple related tasks simultaneously, leveraging shared information to enhance model generalization. Chen *et al.* [31] pioneered a robust multimodal segmentation framework that leverages feature disentanglement, gated fusion, and a reconstruction task, effectively learning

modality-invariant representations and significantly enhancing robustness to missing imaging modalities. Jeong *et al.* [32] later proposed RA-HVED, which uses region-of-interest attention and a joint discriminator for cooperative optimization of segmentation and modality reconstruction. Zhu *et al.* [33] recently presented XLSTM-HVED, incorporating a visual XLSTM and a cross-perception attention module to reinforce inter-task feature interaction and boost performance when modalities are absent. These methods enhance task cooperation, yet careful tuning of inter-task weights remains necessary.

#### 2.2.3. Knowledge Distillation

These methods transfer knowledge from complete-modality models to models operating with missing modalities, thereby substantially enhancing segmentation performance. Wang *et al.* [34] proposed the Adversarial Collaborative Network (ACN), which uses adversarial learning and inter-modal feature-consistency constraints for robust and efficient teacher-to-student knowledge transfer, improving segmentation accuracy under modality absence. Azad *et al.* [35] designed Style-Matching UNet (SMUNet), which explicitly transfers discriminative information through content- and style-matching modules, effectively mitigating performance degradation. Zhu *et al.* [36] further proposed the Multi-Scale Transformer Knowledge Distillation Network (MST-KDNet), which fuses a Transformer architecture with multi-scale feature distillation, enabling rich teacher-student feature interaction and significantly improving generalization under missing modalities. Although these methods bolster robustness, more precise capture of inter-modal differential features warrants further exploration.

### 3. Method

We propose a knowledge-distillation-based, multi-modal 3D UNet segmentation framework. The teacher branch performs high-quality segmentation using complete multi-modal inputs, whereas the student branch incorporates lightweight Adapter modules to learn compensation strategies under modality absence and employs the GARM module to enhance feature representation. Both branches share the LGRM module, which leverages lesion-presence probabilities to suppress false positives and applies a voxel-level mean squared error (MSE) distillation constraint on their outputs, allowing the student model to closely approximate teacher performance while remaining computationally and parameter-efficient.

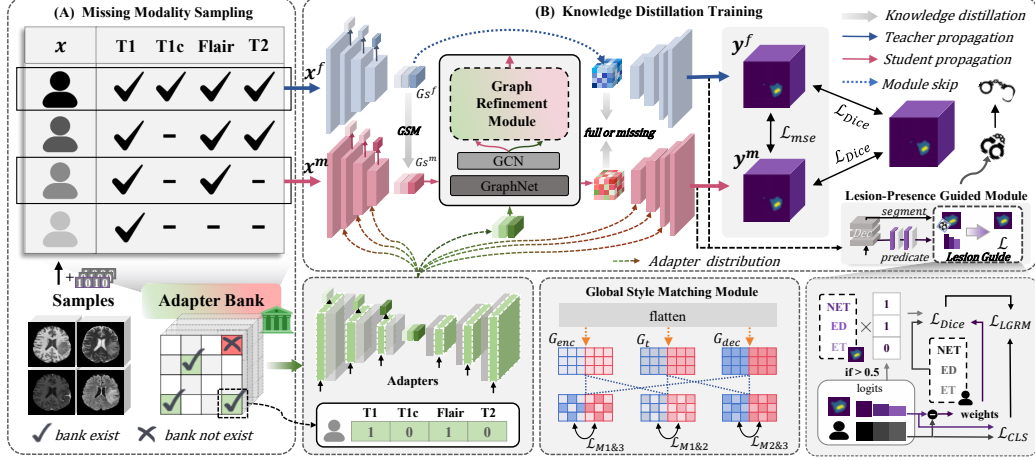


Figure 3: **Framework overview.** (A) **Missing-modality Sampling:** Generates 15 MRI modality combinations and leverages an Adapter Bank to compensate for absent inputs. (B) **Knowledge-distillation Training:** Incorporate BBDM, GARM, and LGRM, with GARM applied exclusively to the student branch.

### 3.1. Bi-Bottleneck Distillation Module

We perform Bi-Bottleneck Distillation Module on the GARM before and after the student model. This knowledge distillation module includes GSME and a teacher-student model discriminator. Due to differences in tissue structure and style features across various MRI modalities, the network decoding process often suffers from information loss in the absence of specific modalities, resulting in a decline in reconstruction quality. To address this issue, we specifically introduce GSME. Concretely, we apply max-pooling to the penultimate encoder features and concatenate them with the bottleneck features; the fused tensor,  $\mathbf{f}_{\text{enc}}$ , is then forwarded to the decoder. The decoder’s first convolutional output,  $\mathbf{f}_{\text{dec}}$ , is further processed by reshaping the spatial dimensions  $H, W, D$  of  $\mathbf{f}_{\text{enc}}, \mathbf{f}_t, \mathbf{f}_{\text{dec}}$  into two-dimensional tensors  $\mathbf{G}_{\text{enc}}, \mathbf{G}_t, \mathbf{G}_{\text{dec}}$ . These tensors are then subjected to a subsequent feature fusion operation:

$$\mathbf{M}_1 = \mathbf{G}_{\text{enc}} \mathbf{G}_{\text{dec}}^T, \quad \mathbf{M}_2 = \mathbf{G}_{\text{enc}} \mathbf{G}_t^T, \quad \mathbf{M}_3 = \mathbf{G}_{\text{dec}} \mathbf{G}_t^T. \quad (1)$$

After obtaining  $\mathbf{M} \in \{\mathbf{M}_1, \mathbf{M}_2, \mathbf{M}_3\}$ , we enforce a MSE distillation loss:

$$\mathcal{L}_{\text{GSME}} = \theta / (4n^2) \sum_{i=1}^3 \sum_{j=1}^n \left( \mathbf{M}_{i,j}^f - \mathbf{M}_{i,j}^m \right)^2, \quad (2)$$

where superscripts  $f$  and  $m$  denote teacher and student features, respectively. Once the enhanced features exit the student’s GARM module, we pair them with the corresponding bottleneck features from the teacher and feed both into a discriminator  $D$  to compute the adversarial loss:

$$\mathcal{L}_{\text{adv}} = \log(1 - D(\mathbf{f}_{\text{GARM}}^f)) + \log(D(\mathbf{f}_{\text{GARM}}^m)). \quad (3)$$

The overall distillation loss for the BBDM is therefore defined as:

$$\mathcal{L}_{\text{BBDM}} = \lambda \mathcal{L}_{\text{adv}} + \theta \mathcal{L}_{\text{GSME}}, \quad (4)$$

where  $\lambda$  and  $\theta$  are balancing hyper-parameters. Joint optimisation of these losses transfers high-level structural knowledge and low-level texture cues from the teacher’s encoder and bottleneck to the student model. Consequently, the student preserves cross-modal path consistency and alignment under missing-modality conditions, significantly enhancing overall reconstruction robustness and accuracy.

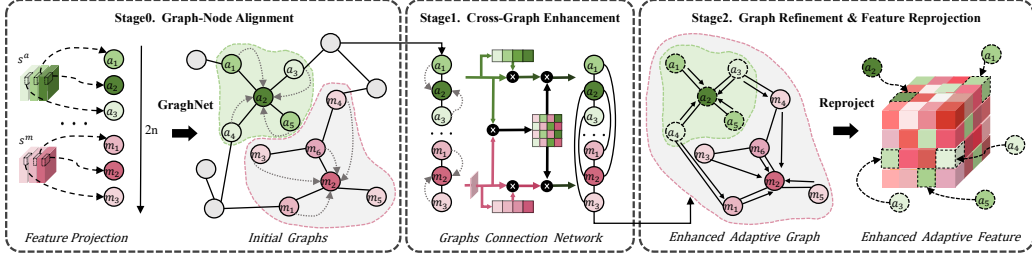


Figure 4: **Graph-guided Adaptive Refinement Module.** **(Stage 0)** Graph-node Alignment, which establishes consistent correspondence between nodes across modality-specific and shared graphs. **(Stage 1)** Cross-graph Enhancement, which facilitates mutual information exchange to enrich node representations. **(Stage 2)** Graph Refinement & Feature Reprojection, which progressively refines node embeddings and projects them back to the feature space for downstream processing.

### 3.2. Graph-guided Adaptive Refinement Module

We have innovatively designed the GARM module to explicitly model the semantic association between Generalization Features (GF) and Combination-aware Features (CF), thereby enhancing feature representation and improving knowledge distillation performance. GARM utilizes a graph neural network structure [37] as a bridge to explicitly connect GF and CF, enabling collaborative reasoning and ultimately projecting enhanced semantic information back into the dense feature space to refine segmentation predictions. In

the specific implementation, we first constructed a training process that simulates missing modalities, generating multiple modality combinations from full-modality inputs using 15 random masking strategies, with missing modalities treated as zero-filled. The processed input  $x \in \mathbb{R}^{H \times W \times D \times C}$  is first processed through 3D convolutions to obtain initial features, then progressively reduced in spatial dimension through three layers of stride=2 downsampling convolutions. In the student model, we introduce an Adapter Bank containing small 3D residual modules, designed for each modality combination except the full modality, which provides flexible modality adaptation capabilities. We insert adapters into the first three downsampling convolutional layers, the last three upsampling convolutional layers, and the bottleneck layer, and fuse all adapter outputs to extract modality combination style features. As shown in Fig. 5, the similarity patterns reveal clear distinctions among adapters while preserving strong specificity to different modality combinations, which, together with the ablation results, underscores the effectiveness of the proposed design in diverse missing-modality scenarios. These features are jointly input into the GARM module, along with global features extracted by 3D convolutions for semantic enhancement. The GARM module consists of three stages: Graph-Node Alignment, Cross-Graph Enhancement, and Graph Refinement & Feature Reprojection.

### 3.2.1. Graph-node Alignment

Given the CF voxel features  $\mathbf{F}_c \in \mathbb{R}^{(8H \times 8W \times 8D \times 32C)}$  from the adapter and the GF features  $\mathbf{F}_g \in \mathbb{R}^{(8H \times 8W \times 8D \times 32C)}$  obtained via 3D convolution, we instantiate two **GraphNet3D** modules (for CF and GF) to parameterize  $K$  learnable anchors and channel-wise bandwidths and to project dense voxels into graph form. Each instance maintains an anchor matrix as the node set and supports HDF5-based initialization of anchors. The structures are:

$$\begin{cases} \mathcal{G}_c = (\mathbf{G}_c, \mathbf{P}_c), & \mathbf{G}_c \in \mathbb{R}^{K \times 32C}, \quad \mathbf{P}_c \in \mathbb{R}^{K \times N}, \\ \mathcal{G}_g = (\mathbf{G}_g, \mathbf{P}_g), & \mathbf{G}_g \in \mathbb{R}^{K \times 32C}, \quad \mathbf{P}_g \in \mathbb{R}^{K \times N}, \end{cases} \quad (5)$$

where  $\mathbf{G}_\star$  stacks the learnable anchors for branch  $\star \in \{c, g\}$  and serves as node features, and  $\mathbf{P}_\star$  is the soft-assignment matrix with  $N=8H \cdot 8W \cdot 8D$ . Additionally, **GraphNet3D** is a learnable projection module that maintains  $K$  trainable anchor vectors (one per graph node) and corresponding channel-wise bandwidth parameters. Given a voxel feature map, it flattens the spatial dimensions, computes channel-wise Gaussian distances between each voxel

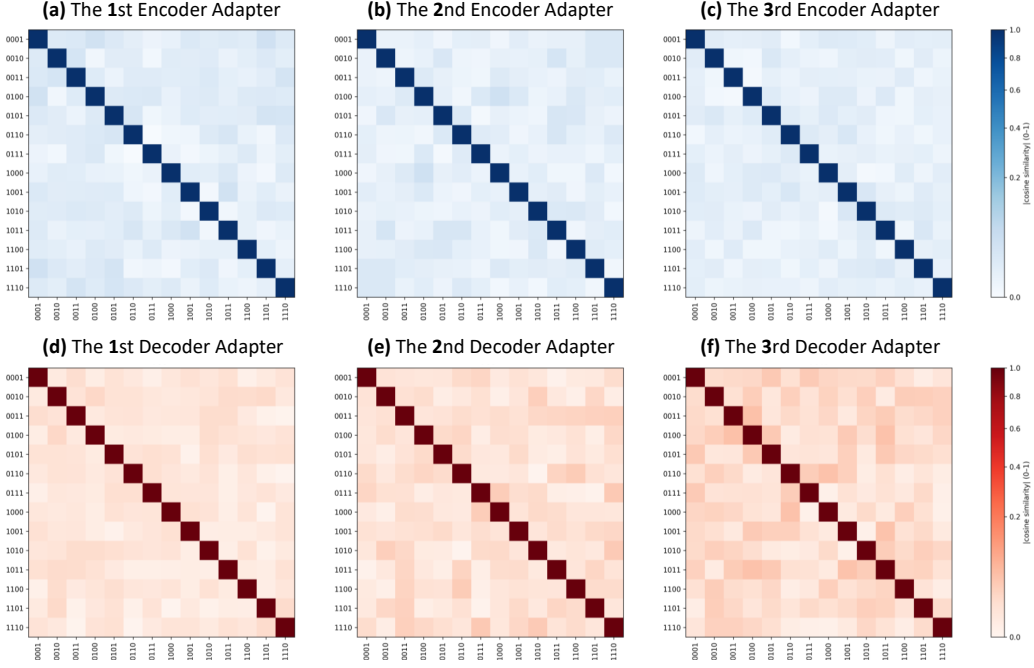


Figure 5: **Cosine similarity heatmaps of adapter parameters.** Each four-digit code denotes available modalities in the order [T1, T1Gd, T2, FLAIR] (1=present, 0=absent). **(a–c)** 1st–3rd encoder adapters, **(d–f)** 1st–3rd decoder adapters. Deeper adapters show higher inter-configuration similarity, indicating convergence toward consistent full-modality feature approximation, while retaining clear modality-combination specificity.

and each anchor, and applies a softmax over nodes to produce a voxel-to-node soft-assignment matrix  $\mathbf{P}$ . This assignment, together with the anchor matrix  $\mathbf{G}$ , defines the graph representation of the input features.

For any voxel feature  $f_i$ , the soft assignment to the  $k$ -th node is computed by a channel-wise Gaussian kernel with learnable bandwidth:

$$\mathbf{P}_{k,i} = \frac{\exp\left(-\| (f_i - \mu_k) \odot \boldsymbol{\sigma}_k^{-1} \|^2_2 / 2\right)}{\sum_{j=1}^K \exp\left(-\| (f_i - \mu_j) \odot \boldsymbol{\sigma}_j^{-1} \|^2_2 / 2\right)}, \quad (6)$$

where  $f_i, \mu_k \in \mathbb{R}^{32C}$  denote the voxel feature and the  $k$ -th learnable anchor,  $\boldsymbol{\sigma}_k \in \mathbb{R}^{32C}$  is a learnable channel-wise bandwidth vector, and  $\odot$  denotes element-wise scaling by  $\boldsymbol{\sigma}_k^{-1}$ . By mapping high-dimensional voxels to a compact  $K$ -node space with learnable anchors and adaptive bandwidths, Graph-node Alignment forms  $\mathbf{P}$  as a locality-preserving correspondence from voxels

to nodes and provides a graph-based abstraction that prepares GF and CF for subsequent cross-graph reasoning with reduced voxel-level redundancy.

### 3.2.2. Cross-Graph Enhancement

To impose explicit one-to-one correspondence prior to holistic graph reasoning, we perform an efficient alignment between the GF and CF graphs. Specifically, a channel-wise linear transformation is applied to the CF graph to harmonize its feature scale with the GF graph:

$$\tilde{\mathbf{G}}_c = \mathbf{W}_c \mathbf{G}_c, \quad \mathbf{W}_c \in \mathbb{R}^{32C \times 32C}. \quad (7)$$

We then establish a comprehensive and fully connected similarity matrix between the GF and CF nodes, and use  $\mathbf{E}$  as the neighborhood to propagate information along GF and CF edges via a graph convolution operation:

$$\begin{aligned} \mathbf{E} &= \mathbf{G}_g^\top \tilde{\mathbf{G}}_c \in \mathbb{R}^{K \times K}, \\ \mathbf{G}'_g &= \text{GCN}(\mathbf{G}_g, \mathbf{E}), \quad \mathbf{G}'_c = \text{GCN}(\tilde{\mathbf{G}}_c, \mathbf{E}), \end{aligned} \quad (8)$$

where GCN refers to a graph convolutional layer that first applies a learnable linear transformation to each node's feature vector, then normalizes the adjacency matrix  $\mathbf{E}$  with a softmax along the neighbor dimension, and finally aggregates transformed features from connected nodes according to these normalized weights. This operation enables information exchange between nodes while respecting the similarity structure encoded in  $\mathbf{E}$ .

By enforcing a one-to-one correspondence between GF and CF nodes through scale-aligned similarity and cross-graph GCN propagation, this block harmonizes the two feature spaces, strengthens correspondence semantics, and improves the stability of distilled representations as well as the accuracy of downstream segmentation under diverse modality combinations.

### 3.2.3. Graph Refinement and Feature Reprojection

To capture complementary semantics from GF and CF, we compute an inter-node cosine similarity matrix to construct a cross-graph adjacency matrix  $\mathbf{A}$  by thresholding the similarity matrix  $\mathbf{S}$  with a threshold value  $\tau = 0.8$ :

$$\mathbf{S} = [\cos(\mathbf{v}_p^g, \mathbf{v}_q^c)]_{p,q=1}^K, \quad \mathbf{v}_p^c \in \mathbf{G}'_c, \quad \mathbf{v}_q^c \in \mathbf{G}'_g, \quad (9)$$

$$\mathbf{A}_{p,q} = \begin{cases} 1, & \mathbf{S}_{p,q} > \tau, \\ 0, & \text{otherwise.} \end{cases}, \quad \mathbf{A}' = (\mathbf{A} + \mathbf{A}^\top)/2, \quad (10)$$

where  $\mathbf{v}$  denotes the node feature vector in  $\mathbf{G}'$ . Then Graph Attention Networks (GAT) [38] are utilized for performing cross-graph aggregation and we build a unified adjacency to facilitate deeper cross-graph interactions:

$$\begin{aligned} \mathbf{G}''_g &= \text{GAT}(\mathbf{G}'_g, \mathbf{A}), \quad \mathbf{G}''_c = \text{GAT}(\mathbf{G}'_c, \mathbf{A}), \\ \mathbf{A}'' &= \begin{bmatrix} \mathbf{A} & \mathbf{A}' \\ \mathbf{A}' & \mathbf{A}^\top \end{bmatrix} \in \mathbb{R}^{2K \times 2K}, \quad \mathbf{A}''' = (\mathbf{A}'' + \mathbf{A}'')^\top / 2. \end{aligned} \quad (11)$$

Joint aggregation is performed on the concatenated node features:

$$\mathbf{G}_{g,c} = [\mathbf{G}'''_g; \mathbf{G}'''_c] = \text{GAT}([\mathbf{G}''_g; \mathbf{G}''_c], \mathbf{A}'''). \quad (12)$$

After the two-stage cross-graph aggregation, the updated node features encode both intra- and inter-graph semantics. These features are projected back to the dense voxel space via the soft-assignment matrices  $\mathbf{P}_c$  and  $\mathbf{P}_g$ , with each node feature distributed to all voxels according to normalized weights  $\mathbf{w}_c$  and  $\mathbf{w}_g$  derived from  $\mathbf{P}_c$  and  $\mathbf{P}_g$ :

$$\begin{aligned} [\mathbf{w}_c; \mathbf{w}_g] &= \text{softmax}([\mathbf{P}_c; \mathbf{P}_g]), \quad \mathbf{P}_{g,c} = \mathbf{P}_g \cdot \mathbf{w}_g + \mathbf{P}_c \cdot \mathbf{w}_c, \\ \mathcal{G}_{g,c} &= (\mathbf{G}'''_c, \mathbf{P}_{g,c}), \quad \mathbf{G}'''_c \in \mathbb{R}^{K \times 32C}, \quad \mathbf{P}_{g,c} \in \mathbb{R}^{K \times N}. \end{aligned} \quad (13)$$

The projected features are further refined by  $1 \times 1 \times 1$  convolutional layers and fused with the original features via residual addition:

$$\mathbf{F} = \mathbf{G}'''_c^\top \mathbf{P}_{g,c}, \quad \mathbf{F}' = \text{Conv}_2(\text{Conv}_1 \mathbf{F} + \text{Conv}_0(\mathbf{F}_g + \mathbf{F}_c)). \quad (14)$$

Finally, a  $1 \times 1 \times 1$  convolution is employed to produce the final segmentation prediction. By explicitly modeling the fine-grained semantic interplay between GF and CF through a graph-based mechanism, GARM effectively integrates generalizable and combination-specific cues, thereby enriching the bottleneck feature representation and markedly enhancing the model's adaptability and expressiveness in multimodal scenarios.

### 3.3. Lesion-Presence Guided Reliability Module

In the multimodal tumor segmentation task, the probability of the presence of different lesion types (Non-Enhancing Tumor Core (NET), ED, ET in BraTS 2018 [39] or Non-Enhancing Tumor Core (NETC), Surrounding Non-enhancing FLAIR Hyperintensity (SNFH), ET in BraTS 2024 [15]) can

provide an important prior for the subsequent segmentation with distillation loss, and often the model misclassifies the tumor. Taking this BraTS 2018 as an example, we embed a lightweight auxiliary classification branch at the end of the decoder, uniformly named LGRM, which introduces only two layers of convolution and a single global average pooling layer, with minimal additional overhead, yet significantly improves Dice and cross-modal consistency. We utilize the  $\mathbf{u}_2$  feature from the decoder’s quadratic upsampling to input the LGRM and obtain the probability vectors. The LGRM consists of two layers of  $3 \times 3 \times 3$  convolution, a BatchNorm, a Global Average Pooling (GAP), and Sigmoid activation:

$$\begin{aligned} \mathbf{z} &= \phi(\text{BN}(\text{Conv}_{3 \times 3 \times 3}(\mathbf{u}_2))), \quad \mathbf{q} = \text{Conv}_{1 \times 1 \times 1}(\mathbf{z}) \in \mathbb{R}^{3 \times D \times H \times W}, \\ \hat{\mathbf{p}} &= \sigma(\text{GAP}(\mathbf{q})) = [\hat{p}_{\text{NET}}, \hat{p}_{\text{ED}}, \hat{p}_{\text{ET}}]^\top \in (0, 1)^3, \end{aligned} \quad (15)$$

where  $\phi(\cdot)$  denotes the relu activation,  $\sigma(\cdot)$  the sigmoid activation, and  $\hat{\mathbf{p}}$  the presence probabilities of the three lesion types. During inference, to suppress false positives, the three-channel segmentation probability map  $\mathbf{S} \in [0, 1]^{B \times 3 \times D \times H \times W}$  is multiplied by the existence mask  $\mathbf{g}$ :

$$\mathbf{g}_{b,i} = \begin{cases} 1, & \hat{p}_{b,i} > 0.5, \\ 0, & \text{otherwise,} \end{cases} \quad b = 1, \dots, B, \quad i \in \{\text{NET, ED, ET}\}, \quad (16)$$

$$\mathbf{S}^* = \mathbf{g} \otimes \mathbf{S},$$

where  $\otimes$  indicates broadcast multiplication along the channel dimension and  $\mathbf{S}^*$  is the final segmentation output. When  $\hat{p}^i \leq 0.5$ , the probability volume for the  $i$ -th class is zeroed out, effectively suppressing false positives in empty regions. Meanwhile, the vector  $\hat{\mathbf{p}}$  is used to derive a probability-weighted segmentation loss and a binary cross-entropy (BCE) classification loss. Let  $\mathbf{y}^{\text{cls}} \in \{0, 1\}^{B \times 3}$  be the hard labels for the three lesion types, obtained by max pooling the ground-truth segmentation masks.

For the complete-modality (full) and missing-modality (miss) branches, the weighting factors are defined as:

$$\mathbf{w}_{\text{full}} = |\hat{\mathbf{p}}_{\text{full}} - \mathbf{y}^{\text{cls}}| + 1, \quad \mathbf{w}_{\text{miss}} = |\hat{\mathbf{p}}_{\text{miss}} - \mathbf{y}^{\text{cls}}| + 1. \quad (17)$$

The purpose of these weights is intuitive: if the network predicts the presence of a lesion with high confidence ( $\hat{\mathbf{p}} \approx 1$ ) but the label is 0, the term  $|\hat{\mathbf{p}} - \mathbf{y}|$

becomes large, the weight increases, and the false-positive error is penalised; conversely, if the network fails to predict a lesion that is actually present ( $\hat{\mathbf{p}} \approx 0$ ,  $\mathbf{y} = 1$ ), the weight likewise increases to penalise the false negative. The weighted Dice losses and binary cross-entropy (BCE) classification losses for the three lesion types are thus:

$$\begin{aligned}\mathcal{L}_{\text{Dice}}^{\text{full}} &= \sum_{i \in \{\text{NET,ED,ET}\}} \mathbf{w}_{\text{full},i}/B \sum_{b=1}^B \text{Dice}(\mathbf{S}_i^{(b)}, \mathbf{Y}_i^{(b)}), \\ \mathcal{L}_{\text{Dice}}^{\text{miss}} &= \sum_{i \in \{\text{NET,ED,ET}\}} \mathbf{w}_{\text{miss},i}/B \sum_{b=1}^B \text{Dice}(\mathbf{S}_{i,\text{miss}}^{(b)}, \mathbf{Y}_i^{(b)}), \\ \mathcal{L}_{\text{CLS}}^{\text{full}} &= \text{BCE}(\hat{\mathbf{p}}_{\text{full}}, \mathbf{y}^{\text{cls}}), \quad \mathcal{L}_{\text{CLS}}^{\text{miss}} = \text{BCE}(\hat{\mathbf{p}}_{\text{miss}}, \mathbf{y}^{\text{cls}}).\end{aligned}\quad (18)$$

Therefore, the overall LGRM loss is formulated as the sum of the probability-weighted Dice terms and the BCE classification terms for both the full-and missing-modality branches:

$$\mathcal{L}_{\text{LGRM}} = \mathcal{L}_{\text{Dice}}^{\text{full}} + \mathcal{L}_{\text{Dice}}^{\text{miss}} + \mathcal{L}_{\text{CLS}}^{\text{full}} + \mathcal{L}_{\text{CLS}}^{\text{miss}}. \quad (19)$$

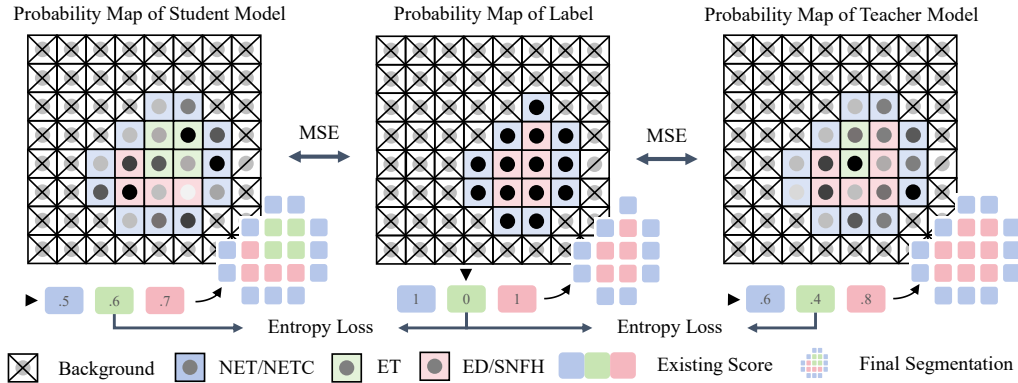


Figure 6: **Lesion-Presence-Guided Reliability Module.** For each slice, voxel-level probability maps from the student (left) and teacher (right) are aligned to the ground-truth label map (centre) with a voxel-wise mean-squared-error. Concurrently, the three lesion classes (NET, ET, ED) are collapsed into existence scores; these scores are matched to the binary presence vector of the label via an entropy loss.

### 3.4. Joint Objective

During the training process, we jointly optimize three types of loss terms to enhance the model's performance, constituting the final total loss function:

$$\mathcal{L}_{\text{joint}} = \lambda_1 \mathcal{L}_{\text{mse}} + \lambda_2 \mathcal{L}_{\text{BBDM}} + \lambda_3 \mathcal{L}_{\text{LGRM}}. \quad (20)$$

Among them,  $\mathcal{L}_{\text{mse}}$  is the teacher-student predictive distillation loss at the voxel level, which guides the student model to quickly fit the predictive distribution of the teacher model, accelerates convergence and enhances the boundary consistency by applying the MSE to the segmentation probability map;  $\mathcal{L}_{\text{BBDM}}$  consists of the MSE of bottleneck features in the GSME module together with the discriminator confrontation loss, which performs the in-depth alignment of structural hierarchies and texture distributions, respectively, to improve the reconstruction quality and detail restoration ability of the student model in the absence of modality;  $\mathcal{L}_{\text{LGRM}}$  introduces the binary cross-entropy loss of classification branch and the probability-weighted Dice loss of segmentation branch based on the existence probability of the lesion in the output of the LGRM module, which explicitly suppresses the false-positives and false-negatives, and especially strengthens the modeling of the boundary ambiguity and the uncertainty region.

The three core losses complement each other at different levels: from shallow output to deep features, from local semantics to global structure, and from deterministic supervision to uncertainty guidance, to optimize the model's segmentation accuracy, distillation efficiency, feature consistency, and discriminative reliability. The hyperparameters  $\lambda_1$ ,  $\lambda_2$  and  $\lambda_3$  control the weight of each loss in the training process to ensure the stability and robustness of the overall optimization process.

## 4. Results

### 4.1. Datasets

#### 4.1.1. BraTS 2024 [15]

This dataset comprises multimodal MRI scans from 1,350 patients, each case including T1, T2, FLAIR, and T1Gd. All images have been resampled to an isotropic resolution of  $1 \text{ mm}^3$ , registered to a standard anatomical template, and pre-processed with skull stripping and related steps. Experienced radiologists manually annotated each case; the segmentation targets encompass three regions: Whole Tumor (WT), Tumor Core (TC), and ET. We

split the dataset 80 % / 20 % into training and testing sets to evaluate the model’s representational capacity and scalability.

#### 4.1.2. BraTS 2018 [39]

This dataset shares the same four MRI modalities and three annotation regions as BraTS 2024 but contains only 285 cases, making it suitable for testing a model’s generalization and resistance to overfitting under limited data. We apply the same 80 % / 20 % training–testing split.

#### 4.2. Experiments Detail

All experiments were conducted on a computing server equipped with NVIDIA Tesla A800 GPUs, and the deep-learning framework was PyTorch 2.4.1. The batch size was fixed at 1. The model was trained for 200 epochs on the BraTS 2024 dataset and for 1,000 epochs on the BraTS 2018 dataset to exploit its limited samples better. Model parameters were updated with the Adam optimizer; the initial learning rate was  $1 \times 10^{-4}$  and decayed to  $1 \times 10^{-5}$  to ensure training stability and efficient convergence. For data pre-processing, all MRI volumes were center-cropped and resampled to an input size of  $160 \times 192 \times 168$  voxels, followed by intensity normalization to promote training stability. During training, we applied several data-augmentation strategies, including random flipping, rotation, and random cropping to improve generalization. During testing, the images were likewise center-cropped to the same dimensions to maintain consistency with the training phase.

#### 4.3. Assessment of Indicators

To comprehensively evaluate the model’s segmentation performance on the BraTS 2024 and BraTS 2018 datasets, we adopted four commonly used metrics: Dice coefficient, Intersection over Union (IoU), Sensitivity, and Hausdorff Distance 95% (HD95). Their definitions are as follows:

$$\begin{aligned} \text{Dice} &= \frac{2|X \cap Y|}{|X| + |Y|}, & \text{IoU} &= \frac{|X \cap Y|}{|X \cup Y|}, & \text{Sensitivity} &= \frac{\text{TP}}{\text{TP} + \text{FN}}, \\ d_{\text{H}}(X, Y) &= \max\{d_{XY}, d_{YX}\} = \max\left(\max_{x \in X} \min_{y \in Y} d(x, y), \max_{y \in Y} \min_{x \in X} d(x, y)\right), \end{aligned} \quad (21)$$

where  $|X \cap Y|$  denotes the number of elements in the intersection of sets  $X$  and  $Y$ , whereas  $|X|$  and  $|Y|$  represent the cardinalities of  $X$  and  $Y$ , respectively;

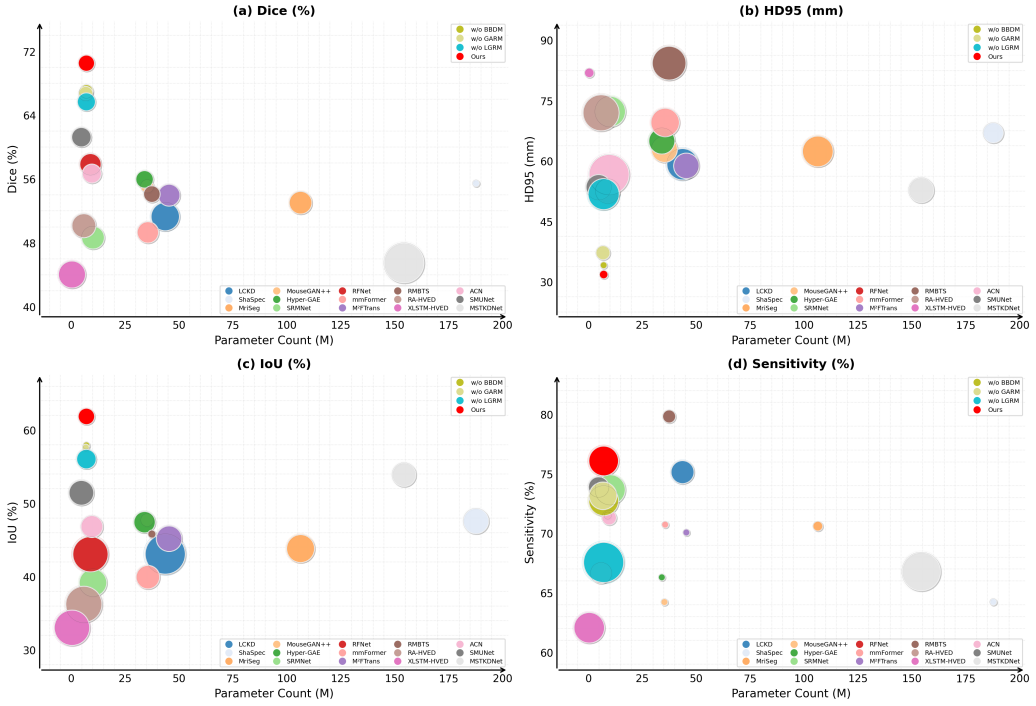


Figure 7: Scatter plots showing the relationship between model performance and parameter count across four evaluation metrics: (a) **Dice (%)**, (b) **HD95 (mm)**, (c) **IoU (%)**, and (d) **Sensitivity (%)**. The proposed method (**Ours**) is highlighted in red.

$x$  and  $y$  are elements of  $X$  and  $Y$ . The symbol  $d$  denotes distance, and HD95 is computed as the 95<sup>th</sup> percentile of the distances between the boundary points of  $X$  and  $Y$ . True Positives (TP) and False Negatives (FN) denote correctly predicted positive voxels and incorrectly predicted negative voxels.

#### 4.4. Comparative Experiments

We conducted systematic comparative experiments by randomly omitting input modalities to mimic clinical modality-missing scenarios, thus creating 15 input configurations encompassing single-, dual-, triple-, and full-modality combinations. As summarized in Tables 1, 2, 3, 4, 5, 6, 7, 8, we compared our method with several mainstream missing-modality brain-tumor segmentation approaches on the BraTS 2024 and BraTS 2018 datasets to verify the effectiveness of the proposed model. Owing to space constraints, this section focuses on the BraTS 2024 results; trends on BraTS 2018 are broadly

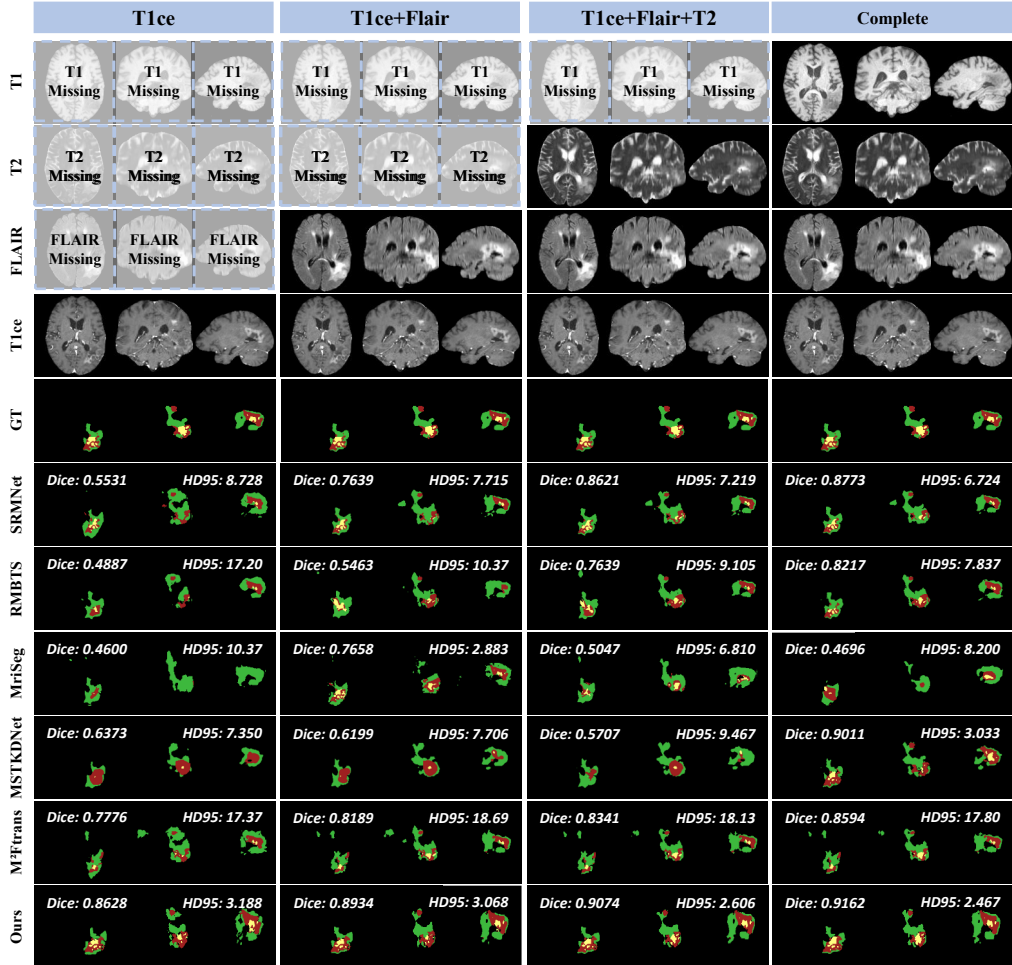


Figure 8: **Qualitative comparation study on the BraTS 2024 dataset.** Visualization of a randomly selected sample from the BraTS 2024 dataset, showcasing segmentation results under different modality-missing combinations across three distinct axial views. The corresponding multimodal MRI sequences and corresponding ground truth are presented, along with outputs of models. Dice and HD95 metrics are displayed for each model-combination pair. From visualizations and metrics, our model (**Ours**) demonstrates superior segmentation accuracy and edge-control ability, with higher Dice values and lower HD95 results across various modality-missing scenarios. Color legend: WT = red + yellow + green, TC = red + yellow, ET = red.

similar. The results show that AdaMM consistently outperforms competing methods under most modality-missing settings, demonstrating superior robustness and segmentation accuracy. First, relative to data-generation methods such as MouseGAN++ [20] and Hyper-GAE [21], AdaMM raises the average single-modality Dice score by 23.55% and 23.74%, respectively, and improves the single-modality IoU score by 14.71% and 17.37%. These findings indicate that, instead of relying on complex generative networks to recover missing modalities, AdaMM leverages the BBDM distillation module to transfer structural and textural knowledge from the teacher model to the student model, achieving better performance without synthesizing additional data and with lower computational overhead. Second, compared with feature-generation methods such as MRISeg [19] and ShaSpec [18], AdaMM reduces the HD95 metric by 31.09mm and 35.7mm and increases Sensitivity by 5.94% and 12.31%. This result confirms that AdaMM’s GSME module aligns structural and style features between teacher and student more effectively, mitigating the information-reconstruction deficiencies caused by contextual absence in feature-generation approaches.

When contrasted with multi-task learning methods such as RA-HVED [32] and RMBTS [31], we observe that these approaches often suffer feature conflicts within task coupling, limiting primary-task performance. By contrast, AdaMM’s LGRM module provides priors for the three tumor regions and effectively enhances target awareness. For example, under the FLAIR-only setting, AdaMM attains a Dice score of 59.91%, exceeding the scores of RA-HVED and RMBTS 31.35% and 37.56%, respectively corresponding to improvements of 28.56 and 22.35 percentage points; the IoU metric rises by 28.88% and 21.65%, indicating superior reconstruction of tumor regions.

Against existing robustness-enhancement methods such as RFNet [28] and M<sup>2</sup>FTrans [30], AdaMM markedly improves feature representation under missing modalities via the GARM module’s graph-neural architecture. Unlike these methods, which directly process the raw incomplete inputs, AdaMM mitigates noise propagation and sample dependence by modeling modality combination relationships through a graph structure. It achieves gains of 76.54% and 31.29 mm in average Sensitivity and HD95, respectively, underscoring its adaptability to detail recovery and boundary detection.

Finally, in comparison with other knowledge-distillation methods such as ACN [34] and SMUNet [35], AdaMM effectively overcomes the modality-distribution inconsistency inherent in conventional distillation. Our GSME with GARM cooperative mechanism enables deep alignment from style fea-

tures to graph-structured knowledge, further elevating distillation quality and segmentation performance. The GARM module conveys cross-modal topological relationships, whereas GSME precisely aligns the global style expressions between teacher and student, jointly ensuring consistent predictions across diverse modality combinations. Fig.8 illustrates the segmentation results of a randomly selected sample from the BraTS 2024 dataset under different combinations, encompassing three distinct axial views.

#### 4.5. Ablation Experiments

To verify the contribution of each module to overall performance, we conducted ablation experiments on the BraTS 2018 and BraTS 2024 datasets, successively removing BBDM, GARM, and LGRM for comparative analysis. Owing to space constraints, this section focuses on the results of BraTS 2024 dataset; trends on BraTS 2018 dataset are broadly similar. As shown in Tables 1, 2, 3, 4, 5, 6, 7, 8 and Fig. 9, eliminating any single component leads to substantial declines in Dice, HD95, Sensitivity, and IoU, demonstrating that all three modules are essential for maintaining accuracy and robustness, and underscoring that their synergistic interaction is critical for ensuring model stability and generalization.

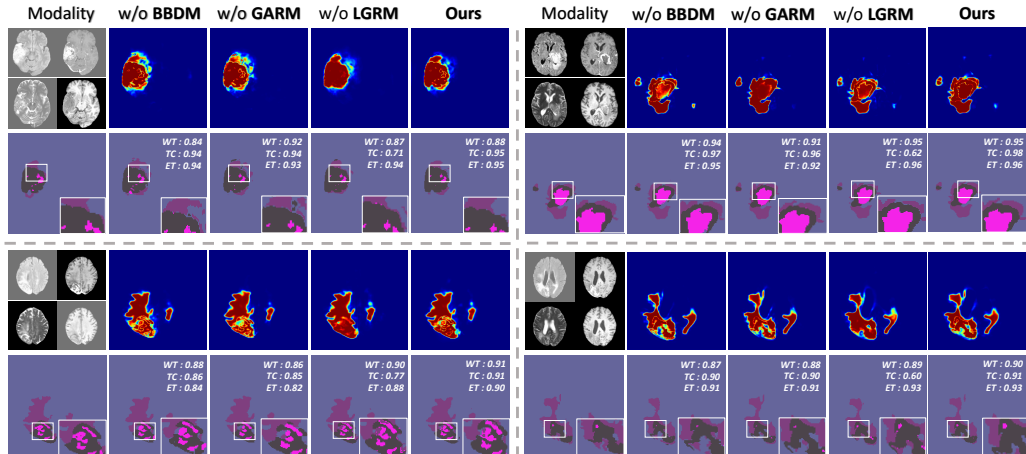


Figure 9: **Qualitative ablation study on the BraTS 2024 dataset.** Input images and ground-truth masks are shown for four modality configurations (T1, T1+T1Gd+T2+FLAIR, T1Gd+T2, and T1+T1Gd+T2). From left to right, the remaining columns present the segmentation outputs and corresponding prediction heatmaps produced by models without BBDM, without GARM, without LGRM, and with the complete model. Dice scores for WT, TC, and ET are reported.

Table 1: Quantitative comparison results measured in DSC (%) on BraTS 2024

Type		Flair	○	○	○	●	○	○	●	○	●	●	●	●	●	○	●	●	Avg.	Std.
WT	LCKD [17]	78.99	<b>79.96</b>	75.62	77.98	78.68	<b>78.45</b>	79.74	79.97	80.78	81.43	82.03	82.55	82.95	<b>82.91</b>	83.28	80.15	2.29		
	ShaSpec [18]	67.13	49.16	41.58	58.18	72.89	72.17	74.82	52.13	64.11	61.14	74.29	76.57	76.03	64.01	76.67	65.39	10.7		
	MriSeg [19]	78.82	55.90	64.28	64.81	<b>81.81</b>	70.84	72.80	<b>81.44</b>	82.16	66.84	73.93	83.04	83.46	<b>83.38</b>	83.74	75.15	8.6		
	MouseGAN++ [20]	64.38	66.95	57.79	61.45	75.35	61.22	70.58	78.98	77.67	66.43	79.47	63.63	65.49	68.77	80.77	69.26	7.22		
TC	Hyper-GAE [21]	75.93	60.91	70.05	66.94	74.82	72.64	75.03	70.91	76.87	60.73	78.07	78.55	77.68	74.77	76.98	72.73	5.62		
	SRMNet [22]	64.75	49.74	43.81	73.66	72.04	58.25	75.50	67.39	79.52	78.60	78.50	79.26	81.72	72.69	81.12	70.44	11.27		
	RFNet [28]	73.38	67.57	68.12	81.22	76.83	70.83	83.09	76.27	83.33	83.87	84.22	83.83	84.50	77.23	84.56	78.59	5.98		
	mmFormer [29]	64.77	46.71	57.19	76.68	67.65	55.83	78.05	68.17	78.83	77.57	77.27	78.86	78.87	67.77	77.96	70.15	9.89		
ET	M <sup>2</sup> FTrans [30]	69.87	58.81	59.42	79.56	73.32	65.57	81.01	73.61	81.71	81.76	82.09	82.17	82.62	74.76	82.70	75.27	8.13		
	RMBTS [31]	68.63	50.67	51.96	63.38	73.62	59.93	76.06	73.62	75.75	75.00	78.82	78.65	78.89	74.60	79.64	70.61	9.34		
	RA-HVED [32]	50.96	80.75	52.13	65.56	<b>83.79</b>	<b>82.75</b>	69.37	58.11	70.42	83.31	83.62	70.05	84.85	84.30	84.86	73.65	11.89		
	XLSTM-HVED [33]	72.18	45.14	49.58	57.87	74.24	54.12	63.18	73.19	74.16	63.16	65.93	74.37	75.80	75.08	75.93	66.26	10.00		
Ours	ACN [34]	68.95	61.95	57.93	79.49	73.23	64.34	81.99	74.27	81.10	81.94	82.08	82.81	81.64	74.69	82.45	75.26	8.08		
	SMUNet [35]	75.20	70.56	69.19	83.64	77.74	72.95	85.17	78.31	84.96	84.81	85.46	85.64	85.40	78.34	85.81	80.21	5.78		
	MSTKDNet [36]	77.29	72.88	73.11	<b>84.76</b>	80.32	74.89	85.35	79.12	<b>86.07</b>	<b>87.17</b>	<b>87.02</b>	<b>85.92</b>	<b>87.45</b>	80.26	<b>86.98</b>	<b>81.91</b>	5.20		
	w/o BBDM	73.35	66.74	68.43	82.40	76.42	70.48	83.97	75.50	83.87	84.42	84.93	83.81	85.01	77.23	84.51	78.74	6.33		
Ours	w/o GARM	73.39	67.20	68.70	82.48	76.67	70.65	83.69	74.94	83.97	84.56	84.73	83.85	84.88	77.49	84.63	78.89	6.19		
	w/o LGRM	78.99	68.93	70.18	82.87	78.04	72.00	84.39	77.83	84.40	84.92	85.23	84.81	85.29	78.74	85.37	80.13	5.16		
	<b>Ours</b>	<b>80.55</b>	<b>74.07</b>	<b>75.72</b>	<b>86.96</b>	81.56	76.94	<b>87.77</b>	<b>81.53</b>	<b>88.15</b>	<b>88.57</b>	<b>88.64</b>	<b>88.32</b>	<b>89.11</b>	81.94	<b>88.69</b>	<b>83.90</b>	5.31		
	LCKD [17]	27.59	27.51	35.91	33.82	33.18	37.08	39.69	41.77	40.57	39.61	41.20	42.47	41.67	42.79	43.73	37.91	5.1		
Ours	ShaSpec [18]	28.52	43.62	32.13	38.08	58.28	58.09	60.74	56.98	52.59	50.17	61.00	63.61	61.32	55.50	62.67	52.22	11.01		
	MriSeg [19]	18.65	50.41	17.08	25.89	55.10	52.45	27.45	23.52	31.36	55.04	62.10	31.27	61.50	60.09	62.72	42.31	16.87		
	MouseGAN++ [20]	24.63	48.28	29.13	21.71	64.70	58.67	50.59	34.63	35.45	60.65	57.16	48.80	59.20	61.42	63.53	47.90	14.42		
	Hyper-GAE [21]	24.87	33.61	39.72	28.28	57.94	57.16	54.87	54.63	<b>59.73</b>	60.99	60.85	59.77	60.85	59.77	62.95	51.09	12.35		
Ours	SRMNet [22]	24.12	41.21	24.84	24.62	52.35	47.04	31.23	27.99	28.29	48.73	57.38	31.65	57.38	54.40	62.92	41.73	14.51		
	RFNet [28]	29.66	57.12	31.02	24.87	62.21	61.54	33.42	34.47	32.53	60.36	63.52	35.32	63.52	64.76	64.01	47.86	15.45		
	mmFormer [29]	26.52	41.08	22.74	22.01	49.27	47.23	26.92	28.95	29.34	51.39	54.81	31.03	53.26	50.63	55.71	39.39	12.41		
	M <sup>2</sup> FTrans [30]	22.85	47.06	25.31	23.66	57.36	55.71	30.72	29.90	27.87	56.97	63.21	31.07	62.53	60.47	60.28	43.43	14.9		
Ours	RMBTS [31]	23.38	41.51	42.49	24.63	41.11	49.56	57.38	60.64	33.26	33.89	57.10	<b>56.99</b>	46.62	62.09	64.26	47.15	13.41		
	RA-HVED [32]	54.57	20.38	10.40	15.86	55.55	21.22	13.19	48.99	<b>57.62</b>	23.03	21.41	58.48	59.78	61.56	63.23	39.02	20.19		
	XLSTM-HVED [33]	13.64	42.89	14.35	10.37	47.93	49.08	14.12	13.83	16.21	46.21	49.17	51.83	47.76	18.63	52.81	32.59	17.17		
	ACN [34]	27.91	24.66	<b>58.74</b>	22.19	31.17	64.46	<b>64.56</b>	<b>64.50</b>	31.18	30.18	67.89	67.72	30.78	65.60	67.79	47.94	18.63		
Ours	SMUNet [35]	26.24	30.32	<b>64.26</b>	28.81	30.43	69.31	<b>67.70</b>	<b>67.98</b>	31.65	31.73	71.14	<b>69.79</b>	32.03	70.97	71.91	51.07	19.66		
	MSTKDNet [36]	36.96	65.76	34.84	34.50	68.33	68.75	37.63	39.22	40.30	65.23	70.75	40.23	67.21	70.27	70.57	54.01	15.03		
	w/o BBDM	44.01	71.24	41.71	<b>42.22</b>	75.52	74.66	46.13	45.96	47.23	<b>76.59</b>	<b>79.72</b>	47.26	<b>76.65</b>	76.24	<b>77.92</b>	<b>61.48</b>	15.63		
	w/o GARM	42.56	<b>72.32</b>	41.24	39.42	<b>76.37</b>	<b>76.27</b>	43.56	43.93	47.45	75.82	77.90	46.53	76.65	77.11	77.25	60.96	14.44		
Ours	w/o LGRM	41.55	69.15	40.37	38.90	73.95	73.19	44.71	43.74	42.93	73.53	76.17	45.82	74.29	<b>76.28</b>	76.04	59.37	15.87		
	<b>Ours</b>	<b>47.94</b>	<b>75.24</b>	45.40	<b>47.77</b>	<b>76.66</b>	<b>77.80</b>	51.00	50.74	51.32	<b>76.86</b>	<b>79.77</b>	51.51	<b>78.24</b>	<b>78.45</b>	<b>78.58</b>	<b>64.49</b>	14.74		
Ours	LCKD [17]	24.44	24.39	33.82	31.36	30.59	34.93	37.83	40.09	38.69	37.60	39.37	40.77	39.85	41.09	42.12	35.80	<b>5.58</b>		
	ShaSpec [18]	27.93	31.76	35.99	26.63	48.7	53.9	48.1	61.39	39.44	55.27	66.43	51.3	57.27	59.16	68.46	48.78	<b>13.11</b>		
	MriSeg [19]	14.93	50.98	13.94	21.82	56.37	53.08	24.07	19.66	28.33	56.81	64.23	28.25	64.2	62.11	65.55	41.62	19.49		
	MouseGAN++ [20]	18.48	49.7	27.37	22.29	58.19	59.03	30.81	45.14	57.37	58.64	59.7	50.81	61.01	61.18	62.04	48.12	15.00		
Ours	Hyper-GAE [21]	12.65	28.06	28.39	20.46	34.58	43.21	<b>62.65</b>	63.21	24.52	43.24	66.17	63.04	53.44	54.46	62.95	44.07	17.57		
	SRMNet [22]	10.91	42.23	11.71	11.1	53.52	48.39	16.71	15.57	14.75	49.49	53.86	17.76	51.82	54.4	54.59	33.79	18.75		
	RFNet [28]	26.3	58.05	27.92	21.93	63.19	62.95	29.92	31.2	29.47	61.73	65.28	32.15	64.45	66.14	65.8	47.1	17.71		
	mmFormer [29]	22.4	41.31	21.79	19.12	50.27	48.06	23.51	25.28	23.86	52.4	56.08	26.76	55.24	52.49	57.53	38.41	14.71		
Ours	M <sup>2</sup> FTrans [30]	22.85	48.2	22.6	23.66	57.36	57.23	26.52	26.98	24.43	58.87	63.21	28.75	62.53	63.51	43.21	17.34			
	RMBTS [31]	23.38	26.19	46.41	24.68	30.37	53.93	57.38	49.29	28.26	27.33	57.54	58.97	59.68	61.23	63.8	44.56	15.22		
	RA-HVED [32]	<b>53.54</b>	15.79	8.83	12.64	57.87	18.06	10.72	49.97	<b>58.07</b>	18.64	17.46	59.75	61.67	61.94	61.86	37.79	22.04		
	XLSTM-HVED [33]	13.86	44.26	14.29	10.02	50.17	50.19	14.44	14.60	14.01	47.62	51.13	52.96	49.90	17.03	54.38	33.26	18.15		
Ours	ACN [34]	25.61	21.23	<b>59.51</b>	19.45	27.27	65.14	<b>65.35</b>	<b>65.14</b>	28.01	26.61	69.42	<b>67.72</b>	27.90	66.33	68.18	46.86	20.52		
	SMUNet [35]	29.75	34.22	<b>63.93</b>	33.36	35.01	67.82	67.7	<b>67.98</b>	35.25	35.59	70.34	<b>68.89</b>	35.46	70.26	71.09	52.44	17.29		
	MSTKDNet [36]	33.98	65.76	32.43	31.87	68.23	69.35	35.16	36.43	37.51	65.23	70.75	38.03	71.16	71.35	71.16	52.94	16.88		
	w/o BBDM	41.67	72.12	39.31	<b>39.54</b>	76.06	<b>75.56</b>	43.31	43.49	44.86	<b>77.22</b>	<b>79.72</b>	44.93	77.26	77.04	<b>78.64</b>	<b>60.72</b>	17.23		
Ours	w/o GARM	40.3	<b>73.3</b>	38.74	36.73	<b></b>														

Table 2: Quantitative comparison results measured in HD95 (mm) on BraTS 2024

Type	Flair	○	○	○	●	○	○	●	○	●	●	●	●	○	●	Avg.	Std.		
		○	○	●	○	○	●	●	○	●	●	●	○	●	●				
		○	●	○	○	●	●	○	○	●	●	●	○	●	●				
		●	○	○	○	●	●	○	○	●	●	●	○	●	●				
WT	LCKD [17]	<b>7.07</b>	<b>6.89</b>	<b>7.28</b>	6.89	<b>6.55</b>	<b>6.70</b>	6.41	<b>6.29</b>	6.11	<b>5.88</b>	<b>5.69</b>	5.54	5.40	<b>5.43</b>	<b>5.32</b>	6.23	<b>0.64</b>	
	ShaSpec [18]	28.84	40.88	47.63	25.32	23.85	22.57	19.72	44.79	23.95	30.51	20.97	16.57	16.76	29.69	14.29	27.09	9.88	
	MriSeg [19]	10.61	23.63	12.72	12.27	8.40	12.97	8.54	8.26	6.48	11.81	9.88	6.23	7.80	6.37	7.22	10.21	4.24	
	MouseGAN++ [20]	27.50	27.02	13.69	21.72	15.61	14.98	13.85	19.90	15.46	12.21	14.62	18.09	16.67	13.94	11.25	17.10	4.78	
	Hyper-GAE [21]	19.00	17.64	24.78	27.01	22.46	22.61	17.70	24.71	13.92	20.19	13.10	13.04	17.92	16.34	14.31	18.98	4.37	
	SRMNet [22]	17.76	34.60	50.23	24.57	13.00	29.53	22.59	18.01	14.20	18.23	17.32	15.49	17.32	14.35	13.37	21.11	9.98	
	RFNet [28]	<b>7.50</b>	12.58	11.69	10.31	7.75	10.59	7.35	<b>6.76</b>	6.68	8.40	7.82	6.22	7.44	7.83	<b>7.47</b>	8.43	<b>1.89</b>	
	mmFormer [29]	16.39	55.86	30.99	18.20	18.31	38.98	14.09	14.40	10.89	19.54	15.97	11.21	11.88	17.62	12.10	20.43	12.00	
	M <sup>2</sup> FTTrans [30]	17.85	27.96	20.37	14.18	12.76	15.70	10.75	10.42	12.15	10.98	10.06	9.36	10.63	10.25	9.06	13.50	4.99	
	RMBTS [31]	26.33	52.62	53.01	23.53	24.43	46.46	19.95	22.67	18.04	25.41	21.79	24.51	23.34	18.34	27.66	11.96	11.34	
	RA-HVED [32]	27.82	12.28	21.76	15.84	6.79	8.39	11.34	13.21	10.99	8.03	6.16	9.51	5.69	5.76	5.45	11.53	6.34	
TC	XLSTM-HVED [33]	27.87	<b>7.72</b>	35.86	28.02	29.27	31.27	25.09	24.81	30.14	27.57	26.00	24.07	22.46	22.71	26.65	6.52		
	ACN [34]	17.60	18.79	18.80	10.91	13.97	18.65	10.94	11.85	10.43	9.62	9.62	8.45	11.24	11.01	9.92	12.79	3.63	
	SMUNet [35]	8.64	15.65	11.81	8.75	10.17	11.37	6.00	8.48	6.71	7.53	7.30	5.63	6.57	8.53	5.55	8.58	2.65	
	MSTKNet [36]	8.25	12.95	11.80	7.39	8.36	11.09	5.31	8.54	5.33	6.17	6.26	<b>5.06</b>	<b>4.80</b>	8.32	6.27	7.73	2.46	
	w/o BBDM	10.70	14.41	12.80	11.32	10.05	10.94	8.29	11.98	6.88	6.76	5.79	6.87	6.93	8.72	7.60	9.34	2.52	
	w/o GARM	10.02	13.08	12.53	<b>6.78</b>	9.54	11.01	6.88	10.29	6.32	6.46	6.09	7.15	7.45	8.44	7.30	8.62	2.23	
	w/o LGRM	11.05	12.82	13.05	7.32	9.60	10.71	7.00	9.17	7.27	7.38	7.14	6.69	6.84	9.51	6.66	8.81	2.15	
	Ours	<b>7.74</b>	9.42	<b>8.31</b>	<b>4.60</b>	<b>5.43</b>	<b>7.74</b>	<b>4.28</b>	7.43	<b>3.40</b>	<b>4.09</b>	<b>3.75</b>	<b>3.98</b>	<b>3.75</b>	<b>5.38</b>	<b>5.04</b>	<b>5.62</b>	1.90	
	LCKD [17]	86.47	91.46	85.20	88.98	89.18	85.27	82.48	80.19	81.88	82.76	81.20	79.52	80.41	79.82	78.47	83.55	<b>3.87</b>	
	ShaSpec [18]	104.95	109.58	97.65	102.02	98.64	94.58	86.54	84.72	82.38	89.67	82.97	87.47	87.15	74.60	58.85	88.85	13.22	
	MriSeg [19]	109.43	89.07	109.16	99.65	85.00	91.95	98.90	103.91	84.12	88.24	72.24	83.67	72.37	70.80	68.53	88.51	15.99	
ET	MouseGAN++ [20]	115.43	109.02	100.73	99.22	79.41	80.71	83.90	95.58	81.13	76.00	67.53	78.87	66.28	68.87	64.56	84.48		
	Hyper-GAE [21]	110.12	92.11	93.48	95.02	96.70	93.53	88.06	94.03	99.06	88.76	78.19	81.62	87.76	78.02	63.35	82.63	14.61	
	SRMNet [22]	111.16	10.32	10.08	105.76	89.02	90.51	93.11	90.75	89.22	82.31	92.51	88.14	85.19	80.78	68.50	91.77	11.71	
	RFNet [28]	89.83	74.04	85.41	97.55	64.45	57.31	73.25	63.85	73.57	66.89	62.02	74.30	60.51	55.98	59.30	74.66	12.56	
	mmFormer [29]	97.35	125.43	110.61	99.33	96.52	109.14	92.58	92.18	85.20	89.49	82.44	85.42	79.79	94.48	73.00	94.13	12.91	
	M <sup>2</sup> FTTrans [30]	88.02	104.19	106.17	95.05	76.97	83.12	85.23	81.53	91.07	72.26	63.80	71.86	64.31	64.34	62.28	82.00	13.30	
	RMBTS [31]	115.96	113.92	138.67	116.04	106.35	117.74	115.17	111.18	109.46	110.02	106.26	111.69	106.87	104.43	103.09	111.97	<b>8.51</b>	
	RA-HVED [32]	86.06	117.79	142.20	132.76	83.36	117.95	139.68	116.13	71.00	124.41	124.46	76.75	70.27	69.91	63.51	102.42	27.58	
	XLSTM-HVED [33]	115.50	116.71	133.08	127.35	96.52	105.12	113.83	113.20	107.51	108.44	103.45	99.34	105.36	101.88	91.84	109.28	16.99	
	ACN [34]	94.26	103.15	70.69	102.24	93.69	66.48	71.62	61.48	95.67	90.95	57.54	<b>53.88</b>	101.33	64.17	57.44	78.20	18.59	
	SMUNet [35]	105.65	83.34	<b>65.37</b>	92.80	89.14	65.48	62.26	<b>59.96</b>	93.31	90.76	59.22	60.72	92.94	58.19	56.45	75.71	16.48	
	MSTKNet [36]	94.05	66.43	90.75	91.87	68.75	63.75	81.12	67.25	76.98	73.94	60.20	84.77	68.31	56.10	60.38	75.58	12.63	
TC	w/o BBDM	<b>67.14</b>	45.62	69.66	<b>60.88</b>	37.24	42.90	56.63	<b>59.09</b>	<b>53.82</b>	<b>33.60</b>	<b>30.20</b>	57.64	<b>34.56</b>	<b>37.56</b>	<b>34.39</b>	<b>48.03</b>	12.84	
	w/o GARM	77.63	<b>42.37</b>	70.06	79.16	<b>35.05</b>	<b>40.11</b>	72.15	69.80	66.97	35.34	<b>32.80</b>	66.58	35.14	<b>37.07</b>	35.27	53.03	13.02	
	w/o LGRM	87.50	64.25	89.60	93.66	55.24	61.03	61.00	82.77	84.95	95.15	59.63	54.93	84.82	56.13	50.87	53.35	72.26	16.82
	Ours	<b>66.98</b>	<b>35.28</b>	<b>68.60</b>	<b>56.10</b>	<b>31.94</b>	<b>33.23</b>	<b>56.53</b>	61.68	<b>52.64</b>	<b>33.21</b>	30.02	60.84	<b>28.67</b>	<b>31.25</b>	<b>32.88</b>	<b>45.32</b>	15.24	
	LCKD [17]	95.13	98.02	90.47	93.98	94.13	89.16	86.39	83.80	85.38	86.19	84.46	82.75	83.61	82.51	80.88	87.79	<b>5.18</b>	
	ShaSpec [18]	105.58	113.93	94.17	95.87	82.21	85.51	87.14	90.73	89.75	78.1	71.17	75.29	71.86	56.64	55.02	14.06		
	MriSeg [19]	111.66	91.51	112.03	103.45	84.43	94.23	99.16	104.04	84.34	85.39	69.84	83.71	69.32	67.96	65.41	88.43	15.16	
ET	MouseGAN++ [20]	97.14	94.31	100.54	99.22	99.78	90.22	96.62	95.58	83.26	85.62	88.12	85.23	73.17	74.65	70.23	88.91	7.73	
	Hyper-GAE [21]	98.06	109.4	100.92	94.22	96.7	93.53	88.06	94.03	99.06	88.76	87.76	74.01	72.46	73.19	69.38	89.3	11.57	
	SRMNet [22]	110.23	115.98	123.98	114.41	87.34	109.16	112.08	110.06	107.69	100.97	90.65	107.51	93.89	88.94	86.86	103.98	11.75	
	RFNet [28]	89.83	74.04	85.41	97.55	64.45	57.31	73.25	63.85	85.41	66.89	62.02	81.54	55.98	59.3	74.5			
	mmFormer [29]	97.35	125.76	107.56	99.33	98.32	109.94	92.34	91.93	84.97	91.04	83.72	84.75	79.79	93.77	74.75	94.13	12.91	
	M <sup>2</sup> FTTrans [30]	88.02	104.19	106.17	95.05	76.97	83.12	85.23	81.53	91.07	72.26	63.8	74.78	64.31	64.34	62.28	80.87	13.85	
	RMBTS [31]	117.18	114.76	138.71	118.13	107.63	117.93	116.7	112.81	110.94	110.02	106.26	111.69	106.87	104.43	104.32	113.23	<b>8.25</b>	
	RA-HVED [32]	92.28	124.48	142.72	132.88	76.46	117.88	134.33	116.05	70.57	124.23	124.91	69.70	63.43	69.46	69.56	101.93	28.29	
	XLSTM-HVED [33]	109.54	119.04	14.68	123.82	94.74	108.86	115.13	111.54	109.37	103.90	102.51	104.47	99.50	93.95	109.75	11.46		
	ACN [34]	94.07	103.15	70.69	102.28	98.66	66.48	71.62	61.48	95.67	97.43	54.27	<b>53.88</b>	99.46	64.17	58.36	78.89	19.05	
	SMUNet [35]	107.62	87.29	67.15	95.67	97.09	59.49	76.06	66.32	75.53	92.98	58.62	57.55	95.55	56.33	56.0	76.23	19.02	
	MSTKNet [36]	92.54	66.43	90.75	91.87	68.75	63.75	81.12	82.24	88.26	73.94	60.2	84.77	68.31	56.1	58.69	74.90	12.65	
TC	w/o BBDM	64.33	41.83	<b>66.88</b>	<b>58.08</b>	34.03	39.64	<b>53.87</b>	<b>55.84</b>	<b>51.12</b>	<b>30.33</b>	<b>27.0</b>	54.94	<b>31.38</b>	34.35	<b>31.24</b>	<b>44.99</b>	13.02	
	w/o GARM	74.75	<b>39.09</b>	67.27	76.05	<b>31.89</b>	<b>36.87</b>	69.37	66.94	64.01	32.15	29.56	63.63	32.03	<b>33.87</b>	32.07	49.97	18.06	
	w/o LGRM	92.93	70.73	94.94	94.94	57.79	63.63	92.82	98.86	90.44	56.58	55.99	88.63	55.83	47.79	53.04	74.23	18.23	
	Ours	<b>64.19</b>	<b>34.75</b>	<b>65.64</b>	<b>53.13</b>	<b>31.2</b>	<b>30.02</b>	<b>53.47</b>	<b>54.33</b>	<b>56.35</b>	<b>30.03</b>	<b>26.66</b>	<b>58.05</b>	<b>28.23</b>	<b>28.09</b>	<b>29.71</b>	<b>42.94</b>	1	

Table 3: Quantitative comparison results measured in IoU (%) on BraTS 2024

Type	Flair	○	○	○	●	○	○	●	○	●	●	●	●	○	●	Avg.	Std.	
	T1	○	○	●	○	○	●	●	●	○	○	●	●	●	○			
	T1c	○	●	○	○	●	●	○	○	○	●	●	●	●	○			
	T2	●	○	○	○	●	○	○	●	○	○	●	●	●	●			
WT	LCKD [17]	69.49	67.03	65.38	68.36	69.20	68.87	70.56	70.80	71.87	72.73	73.52	74.22	74.76	74.68	75.17	71.11	2.94
	ShaSpec [18]	67.13	49.16	41.58	58.18	72.89	72.17	74.82	52.13	64.11	61.14	74.29	76.57	76.03	64.01	76.67	65.39	10.70
	MriSeg [19]	67.66	41.34	50.11	50.79	71.64	57.27	59.8	71.04	72.08	52.93	61.15	73.11	73.88	73.48	74.29	63.37	10.43
	MouseGAN++ [20]	54.28	51.98	48.5	57.09	67.37	51.35	61.96	71.46	70.8	56.91	72.17	56.22	56.67	60.22	73.54	60.7	8.07
	Hyper-GAE [21]	58.25	51.85	50.85	57.09	63.28	62.78	64.25	61.05	70.63	68.62	67.52	70.51	68.65	67.28	70.82	63.56	6.37
	SRMNet [22]	50.33	35.91	31.4	61.66	58.53	44.49	63.81	53.6	68.26	67.7	67.64	68.05	71.32	59.67	70.56	58.19	12.20
	RFNet [28]	60.04	53.37	54.3	70.68	64.45	57.31	73.25	63.75	74.74	74.41	74.89	74.73	75.29	65.19	75.38	67.35	7.80
	mmFormer [29]	50.27	33.0	42.91	64.68	53.38	41.44	66.14	53.87	67.12	65.74	65.15	67.03	67.1	53.5	65.82	57.14	10.85
	M <sup>2</sup> FTrans [30]	55.97	44.32	46.02	68.78	59.93	51.77	70.63	60.61	71.38	71.45	71.86	71.93	72.45	61.79	72.53	63.43	9.65
	RMBTS [31]	55.09	36.53	37.68	49.27	60.7	45.53	63.89	60.73	63.74	62.91	67.38	67.24	67.69	61.87	68.61	57.92	10.38
XLSTM	RA-HVED [32]	36.44	69.13	37.49	50.61	73.22	71.84	54.71	43.49	55.92	72.74	73.13	55.75	74.70	73.90	74.73	61.19	13.72
	XLSTM-HVED [33]	59.17	31.38	35.52	43.53	61.65	39.55	48.88	60.57	61.25	49.01	51.75	61.93	63.52	62.53	63.64	52.93	10.68
	ACN [34]	55.12	47.67	43.29	68.38	60.17	50.02	71.62	61.48	70.29	71.53	71.79	72.75	71.09	62.11	72.28	63.31	9.72
	SMUNet [35]	62.28	56.93	55.07	73.58	65.47	59.49	76.06	66.23	75.58	75.29	76.47	76.65	76.03	66.39	76.85	69.22	7.66
	MSTKDNNet [36]	64.73	59.04	59.64	75.16	68.75	61.72	76.06	67.25	76.98	78.64	78.61	76.74	79.05	68.75	78.49	71.31	7.16
	w/o BBDM	59.98	52.2	54.4	71.94	63.87	56.57	74.22	62.82	73.86	74.96	75.6	73.86	75.65	65.01	75.05	67.33	8.22
	w/o GARM	59.93	52.84	54.56	72.07	64.19	56.85	73.78	63.05	73.95	75.11	75.24	73.67	75.43	65.17	74.79	67.38	8.01
	w/o LGRM	62.39	54.67	56.35	72.37	65.9	58.41	74.43	65.46	74.29	75.48	75.84	74.84	75.78	66.75	75.83	68.59	7.44
	Ours	66.77	60.43	61.88	77.94	70.22	64.07	79.22	69.1	79.72	80.46	80.58	79.9	81.23	70.87	80.67	73.54	7.34
	LCKD [17]	20.14	19.96	28.07	26.11	25.43	29.34	31.93	31.04	32.32	32.80	31.82	33.43	34.71	33.89	35.04	35.99	30.18
TC	ShaSpec [18]	16.68	32.63	16.81	14.68	40.23	38.75	42.72	24.99	31.68	38.56	47.03	43.30	48.74	43.17	52.20	35.48	11.75
	MriSeg [19]	12.57	41.27	10.89	18.39	46.09	43.50	19.61	16.13	23.71	46.21	55.90	23.60	52.83	51.25	54.04	34.24	16.02
	MouseGAN++ [20]	38.1	41.16	32.01	36.77	41.55	39.54	43.94	47.67	45.15	44.35	45.06	47.98	49.74	45.06	50.96	43.27	4.98
	Hyper-GAE [21]	13.94	38.47	20.08	16.77	39.59	42.30	41.94	36.77	42.91	29.58	48.05	51.71	54.62	49.10	56.78	37.83	11.90
	SRMNet [22]	26.26	33.24	26.98	16.59	44.25	39.40	10.35	19.36	18.82	40.27	44.81	14.40	43.39	43.84	43.84	26.99	13.18
	RFNet [28]	16.48	41.72	15.25	11.13	44.04	43.95	18.75	15.24	44.03	43.06	44.08	16.84	45.52	44.62	45.65	31.44	13.18
	mmFormer [29]	19.70	31.88	20.37	16.47	40.07	38.08	20.32	22.09	22.13	42.30	45.84	23.76	44.12	41.49	46.65	31.68	10.89
	M <sup>2</sup> FTrans [30]	19.94	37.92	19.76	22.28	46.86	46.82	24.45	23.20	21.55	50.05	51.76	22.27	54.55	53.69	51.44	35.97	13.35
	RMBTS [31]	16.94	22.01	31.91	18.53	35.80	39.73	53.43	53.66	24.36	24.44	44.47	55.56	43.43	56.75	57.44	38.56	14.33
	RA-HVED [32]	31.63	10.62	29.69	10.12	35.97	11.42	8.17	34.87	34.67	14.23	13.07	35.57	36.85	38.60	38.53	24.04	12.82
ET	XLSTM-HVED [33]	6.77	33.45	3.95	5.09	35.75	37.93	5.68	6.37	8.93	36.05	38.44	40.06	37.57	8.96	39.93	23.00	15.52
	ACN [34]	19.90	17.25	48.87	15.47	22.51	54.84	54.93	54.44	22.40	21.91	58.56	58.40	21.76	56.37	58.72	39.09	17.92
	SMUNet [35]	20.65	25.33	53.85	24.40	25.96	58.26	58.61	58.38	25.83	26.80	61.06	59.78	26.04	60.96	62.45	43.22	17.19
	MSTKDNNet [36]	28.25	57.50	26.47	26.22	60.42	61.02	29.20	30.38	31.28	57.55	62.50	31.28	59.23	62.58	62.95	45.79	15.82
	w/o BBDM	36.11	63.14	34.48	34.80	67.64	67.02	38.09	37.87	38.88	68.81	71.21	38.94	68.93	68.34	70.39	53.64	15.68
	w/o GARM	34.88	64.10	33.52	32.05	68.43	68.58	35.53	35.90	39.05	67.96	70.17	38.11	68.85	69.30	69.43	53.06	16.47
	w/o LGRM	31.80	61.09	30.58	29.00	66.45	65.87	34.57	33.74	32.72	65.98	69.36	35.61	66.92	69.24	50.78	17.19	
	Ours	39.87	67.38	37.77	39.91	68.53	70.17	42.47	42.77	42.88	68.73	71.41	42.94	70.76	71.06	71.31	56.45	15.43
	LCKD [17]	16.89	16.78	25.91	23.60	22.75	27.09	29.98	32.22	30.80	29.68	31.46	32.85	31.90	33.16	34.20	27.95	5.47
	ShaSpec [18]	33.24	44.58	34.27	25.20	42.98	44.20	34.60	38.25	25.65	50.71	50.23	52.75	55.06	38.84	57.42	41.87	9.81
	MriSeg [19]	9.58	41.95	8.31	14.70	47.55	44.28	16.54	12.81	20.94	48.23	55.90	20.85	55.84	53.52	57.33	33.89	18.55
XLSTM	MouseGAN++ [20]	19.06	39.47	12.36	21.62	41.75	30.16	44.43	47.61	46.34	49.33	47.37	45.64	50.88	41.07	51.25	39.22	12.02
	Hyper-GAE [21]	22.34	38.69	32.62	19.47	48.50	42.61	42.34	39.63	23.52	40.94	50.85	51.71	54.62	49.10	56.78	40.91	11.45
	SRMNet [22]	8.81	32.27	9.40	9.18	43.13	38.09	14.13	11.58	11.74	39.64	43.39	14.40	41.42	43.83	43.84	32.37	12.96
	RFNet [28]	13.33	42.21	11.59	11.13	44.63	45.01	15.05	15.24	14.99	44.03	45.52	16.84	44.62	45.91	45.65	30.38	15.38
	mmFormer [29]	16.21	31.98	20.02	14.26	41.00	38.90	17.54	19.01	17.49	43.30	47.09	20.01	46.06	43.34	48.42	30.98	12.92
	M <sup>2</sup> FTrans [30]	18.66	39.05	17.69	20.84	48.34	48.42	21.17	20.94	19.16	50.05	54.55	22.27	52.50	53.69	54.76	36.14	15.45
	RMBTS [31]	18.94	32.72	32.96	22.25	36.68	39.96	45.36	45.59	26.61	35.46	55.62	57.37	48.44	57.79	58.56	40.95	12.64
	RA-HVED [32]	32.81	8.46	5.20	7.64	37.01	8.99	6.35	36.34	35.57	10.49	8.91	37.26	37.29	39.28	39.14	23.44	14.44
	XLSTM-HVED [33]	5.13	35.15	2.48	3.84	37.54	39.79	4.15	4.67	6.76	37.79	40.40	41.94	39.32	6.45	41.81	23.15	17.28
	ACN [34]	17.96	14.28	49.84	13.12	18.61	55.61	55.78	55.15	19.22	18.28	60.31	58.37	19.07	57.33	58.99	38.13	19.74
ET	SMUNet [35]	17.11	21.61	54.25	19.92	20.94	60.08	59.86	59.04	22.38	22.91	61.94	60.53	22.67	61.77	62.87	41.86	19.57
	MSTKDNNet [36]	25.22	57.40	24.18	23.66	60.16	61.60	26.74	27.53	28.36	57.09	63.13	28.99	58.75	63.61	63.51	44.66	17.25
	w/o BBDM	33.83	63.94	32.23	32.27	68.01	67.89	35.16	35.33	36.43	69.30	72.00	36.46	69.39	69.07	71.01	52.82	17.23
	w/o GARM	32.69	65.06	31.24	29.61	69.06	69.77	32.86	33.48	36.60	68.67	71.32	35.58	69.53	70.30	70.41	52.41	18.13
	w/o LGRM	27.34	60.11	26.18	25.04	65.85	65.87	30.46	29.45	28.33	65.98	69.07	31.50	69.44	70.01	48.79	17.96	
	Ours	37.03	67.48	35.26	37.16	69.48	71.02	39.92	39.90	40.27	69.47	72.21	40.22	70.75	71.65	72.01	55.60	16.62

Table 4: Quantitative comparison results measured in Sensitivity (%) on BraTS 2024

Type	Flair	○	○	○	●	○	○	●	○	●	●	●	●	●	○	●	●	Avg.	Std.
WT	LCKD [17]	81.27	78.69	77.94	80.76	81.36	80.88	82.23	82.45	83.38	84.01	84.51	85.05	85.47	<b>85.39</b>	85.74	82.61	2.38	
	ShaSpec [18]	60.16	54.78	59.9	54.96	58.21	55.78	60.61	47.87	63.99	67.11	71.06	73.1	76.71	73.27	76.88	63.63	8.66	
	MriSeg [19]	69.23	64.8	66.91	66.03	69.66	67.52	67.73	69.99	69.05	65.89	66.75	69.57	69.64	69.52	69.91	68.15	1.67	
	MouseGAN++ [20]	65.5	65.21	62.63	62.37	67.58	64.67	66.52	67.53	68.12	65.68	68.08	64.51	64.2	65.34	68.48	65.76	1.87	
XLSTM-HVED	Hyper-GAE [21]	64.64	57.78	57.11	63.29	64.94	64.3	65.85	64.27	68.29	67.5	66.41	64.41	74.97	70.26	74.8	66.96	3.24	
	SRMNet [22]	81.22	77.4	78.92	<b>90.12</b>	79.38	77.44	<b>90.89</b>	83.66	89.59	89.55	90.31	90.12	89.04	81.77	89.74	85.28	5.20	
	RFNet [28]	68.77	67.99	67.67	69.91	69.28	68.59	70.22	69.01	70.38	70.51	70.57	70.35	70.63	69.34	70.62	69.59	<b>0.97</b>	
	mmFormer [29]	68.03	67.18	66.76	68.84	69.59	68.55	69.96	69.31	69.86	70.37	70.82	70.39	70.76	69.94	70.96	69.42	<b>1.26</b>	
	M <sup>2</sup> FTrans [30]	67.43	67.27	63.13	68.95	69.17	66.45	68.91	67.53	69.61	70.04	69.83	69.46	70.22	68.87	70.08	68.46	1.81	
	RMBTS [31]	74.44	74.74	<b>82.11</b>	79.79	80.29	<b>81.35</b>	86.99	80.31	84.66	86.52	88.22	87.15	87.29	83.0	88.17	83.00	4.40	
	RA-HVED [32]	49.93	<b>83.32</b>	46.95	66.78	<b>83.01</b>	<b>83.87</b>	67.35	55.33	69.11	84.77	84.76	66.93	85.09	83.36	84.76	73.02	13.26	
	ACN [34]	77.35	45.86	54.27	61.87	81.30	54.59	69.78	82.36	79.34	68.64	72.21	83.10	81.78	82.97	83.88	71.95	12.05	
	SMUNet [35]	74.55	69.67	69.28	82.19	77.94	73.59	84.86	78.62	84.25	83.79	85.65	85.65	84.46	79.51	86.36	80.02	5.68	
	MSTKDNet [36]	79.3	74.65	75.58	87.65	82.66	78.21	89.14	82.68	<b>89.73</b>	<b>90.47</b>	<b>91.28</b>	<b>91.02</b>	<b>91.15</b>	<b>84.0</b>	<b>92.22</b>	<b>85.32</b>	5.93	
TC	w/o BBDM	77.52	69.89	72.07	86.01	80.81	73.98	86.29	80.27	86.2	87.32	87.65	86.82	87.45	81.0	88.28	82.10	6.00	
	w/o GGRAM	76.15	68.67	72.36	84.42	79.34	72.94	85.91	79.59	85.46	85.98	87.07	86.83	87.12	80.4	87.37	81.31	6.05	
	w/o LGRM	78.97	71.56	74.15	87.0	82.48	76.21	88.11	81.76	88.28	88.82	88.73	89.13	90.22	82.75	88.99	83.81	5.92	
	Ours	<b>81.84</b>	76.09	76.36	<b>90.14</b>	<b>83.07</b>	78.27	<b>90.92</b>	<b>83.96</b>	<b>89.95</b>	<b>90.68</b>	<b>91.97</b>	<b>91.60</b>	<b>91.36</b>	83.91	<b>92.33</b>	<b>86.16</b>	5.97	
	LCKD [17]	62.05	63.59	69.99	<b>69.18</b>	68.17	70.77	72.71	74.23	<b>73.35</b>	72.57	73.66	74.59	73.84	74.58	75.30	71.24	3.89	
	ShaSpec [18]	64.64	57.78	57.11	63.29	64.94	64.3	65.85	64.27	68.29	67.5	66.41	66.41	74.97	70.26	74.8	66.05	4.81	
	MriSeg [19]	66.54	73.42	68.98	69.34	74.28	74.72	69.99	68.52	68.69	75.16	74.68	74.68	74.73	75.16	71.87	<b>3.10</b>		
	MouseGAN++ [20]	63.63	60.46	61.46	59.93	63.88	61.09	64.35	64.18	63.8	61.63	62.99	61.42	62.99	71.49	70.75	63.51	3.28	
	Hyper-GAE [21]	63.07	63.29	61.43	68.71	69.06	63.22	64.01	64.22	67.66	68.32	69.0	70.25	71.09	69.75	71.29	66.96	<b>3.24</b>	
	SRMNet [22]	58.53	<b>83.56</b>	50.05	57.29	81.66	83.03	55.49	64.94	61.87	70.58	72.24	72.24	77.14	79.65	82.28	66.10	17.83	
ET	RFNet [28]	68.5	76.04	67.66	67.4	75.81	76.07	69.53	68.88	69.04	75.73	75.91	69.97	75.75	75.92	72.54	3.63		
	mmFormer [29]	<b>68.15</b>	75.53	62.99	65.61	76.38	75.79	66.81	67.44	68.08	74.94	75.39	68.19	75.49	76.32	75.67	71.52	4.63	
	M <sup>2</sup> FTrans [30]	64.87	75.61	65.81	63.64	75.72	75.54	66.2	66.85	66.34	75.1	75.63	67.67	75.32	75.65	75.64	71.04	4.87	
	RMBTS [31]	63.31	69.46	<b>73.65</b>	<b>78.07</b>	73.78	75.52	<b>82.72</b>	71.11	<b>79.09</b>	<b>83.84</b>	<b>85.22</b>	<b>81.99</b>	83.61	76.74	84.23	<b>77.49</b>	6.18	
	RA-HVED [32]	<b>68.54</b>	56.77	44.83	48.24	72.57	55.33	46.17	71.06	71.72	61.00	57.41	71.35	74.53	74.67	74.79	63.27	10.66	
	XLSTM-HVED [33]	36.95	71.84	29.30	35.17	68.92	75.90	34.57	34.12	42.41	74.31	77.78	77.28	73.86	39.84	77.37	56.64	19.56	
	ACN [34]	51.91	48.95	71.93	48.65	57.66	77.73	77.57	<b>76.23</b>	57.30	63.92	81.73	77.88	61.76	78.98	80.38	<b>73.21</b>	8.39	
	SMUNet [35]	58.98	57.02	<b>74.73</b>	56.28	61.48	78.79	<b>78.45</b>	<b>79.30</b>	63.80	61.61	81.93	<b>80.59</b>	63.65	81.45	82.73	70.72	9.99	
	MSTKDNet [36]	44.05	67.05	43.52	41.69	70.07	71.45	45.54	47.72	46.83	67.86	72.67	73.39	72.63	73.39	58.84	12.71		
	w/o BBDM	54.04	79.42	53.39	50.87	<b>83.78</b>	83.27	52.87	54.10	53.37	<b>84.31</b>	<b>85.15</b>	53.80	83.76	82.77	<b>84.74</b>	69.31	15.13	
ET	w/o GARM	55.95	80.18	52.34	51.85	<b>84.37</b>	<b>84.27</b>	54.57	55.70	57.60	83.44	84.67	56.25	<b>84.36</b>	<b>84.62</b>	84.14	70.29	14.50	
	w/o LGRM	43.45	71.09	41.56	39.47	75.26	74.64	45.85	44.90	44.62	75.12	77.89	46.83	75.70	78.16	77.96	60.83	16.09	
	Ours	58.86	<b>81.95</b>	58.30	57.29	82.70	<b>84.00</b>	59.61	62.45	60.58	83.64	85.11	60.75	<b>85.15</b>	<b>84.37</b>	<b>85.51</b>	72.68	12.23	
	LCKD [17]	61.30	63.27	69.99	<b>69.35</b>	68.32	71.11	73.21	74.78	73.84	73.11	74.30	75.29	74.51	75.28	76.04	71.58	4.3	
	ShaSpec [18]	61.92	59.80	57.41	51.00	52.37	64.33	63.18	65.15	63.82	58.05	62.51	70.70	71.68	68.59	74.58	63.01	6.49	
	MriSeg [19]	66.00	74.11	67.59	68.29	74.95	75.34	68.91	67.42	68.16	75.78	75.25	67.90	76.16	74.90	75.83	71.77	<b>3.83</b>	
	MouseGAN++ [20]	63.41	61.71	62.39	56.26	64.89	62.08	65.49	64.89	63.98	62.89	64.30	62.41	62.78	66.60	66.64	63.38	<b>2.44</b>	
	Hyper-GAE [21]	63.07	65.29	66.43	61.71	67.46	63.22	63.07	63.22	65.66	63.32	67.00	64.25	68.09	63.75	69.29	64.99	2.16	
	SRMNet [22]	45.41	<b>83.19</b>	45.23	40.37	81.77	83.07	50.94	51.19	46.11	81.23	83.11	51.58	82.04	82.87	83.46	69.58	10.96	
	RFNet [28]	<b>68.02</b>	76.20	66.88	67.02	75.98	76.26	68.65	68.19	68.49	75.92	76.07	69.17	75.93	76.13	76.11	<b>72.33</b>	4.03	
	mmFormer [29]	66.82	75.85	63.04	65.33	76.57	76.14	66.28	66.49	75.20	75.66	67.01	75.57	76.53	75.79	71.26	5.06		
	M <sup>2</sup> FTrans [30]	64.49	75.66	65.43	63.51	75.87	75.73	65.32	66.01	65.14	75.02	75.56	66.33	75.17	75.83	75.50	70.70	5.21	
ET	RMBTS [31]	65.62	70.12	<b>75.45</b>	<b>79.38</b>	74.56	76.72	<b>84.67</b>	73.38	<b>81.00</b>	<b>84.80</b>	<b>86.60</b>	<b>84.01</b>	<b>84.48</b>	77.98	<b>85.55</b>	<b>78.95</b>	6.08	
	RA-HVED [32]	<b>71.37</b>	55.28	44.67	45.92	75.20	53.34	44.65	73.98	<b>74.32</b>	57.34	54.06	74.51	76.72	76.89	77.05	63.69	12.65	
	XLSTM-HVED [33]	35.14	75.17	28.26	33.88	71.78	79.48	32.91	32.53	39.96	77.03	81.14	80.66	76.87	36.71	80.82	57.49	22.02	
	ACN [34]	51.38	46.34	74.68	47.38	57.01	80.60	79.37	<b>79.31</b>	56.48	61.55	83.82	80.23	60.66	82.33	83.11	67.51	11.83	
	SMUNet [35]	58.47	55.36	<b>76.08</b>	55.46	60.51	80.60	<b>79.70</b>	<b>80.83</b>	62.58	59.88	83.51	<b>81.72</b>	61.72	83.33	84.18	70.93	11.32	
	MSTKDNet [36]	38.74	65.91	39.51	36.84	68.91	70.96	40.65	42.70	42.01	66.49	72.38	44.40	67.68	72.67	72.85	56.18	14.71	
	w/o BBDM	49.56	79.13	48.60	45.94	<b>82.82</b>	82.69	48.03	49.40	48.81	83.80	84.63	49.40	83.05	82.08	83.93	66.79	17.13	
	w/o GARM	51.31	79.98	47.31	46.42	<b>83.87</b>	<b>84.11</b>	49.63	50.99	52.82	83.13	84.67	51.49	83.91	<b>84.21</b>	83.96	67.85	16.80	
	w/o LGRM	37.87	69.40	36.38	34.55	74.15	74.16	40.52	39.49	39.12	74.75	77.27	41.87	75.03	77.97				

Table 5: Quantitative comparison results measured in DSC (%) on BraTS 2018

Type		Flair	○	○	○	●	○	○	●	○	●	●	●	●	●	○	●	●	Avg.	Std.
WT	LCKD [17]	76.18	71.32	70.72	74.31	75.28	74.93	76.73	77.26	78.31	79.16	79.94	80.59	81.08	81.12	81.56	77.23	<b>3.35</b>		
	ShaSpec [18]	78.89	42.74	43.99	66.55	81.97	82.15	82.34	56.70	69.91	71.98	83.19	83.53	83.75	73.32	84.41	72.36	13.70		
	MriSeg [19]	82.90	68.58	78.07	47.89	85.90	82.33	80.67	85.82	85.60	66.20	80.71	86.66	87.86	87.85	87.69	79.65	10.63		
	MouseGAN++ [20]	66.67	75.83	60.28	60.51	79.07	79.71	71.36	70.63	68.60	79.88	79.10	73.00	81.20	80.14	82.81	73.92	7.13		
XLSTM-HVED	Hyper-GAE [21]	73.99	65.36	67.59	74.44	72.81	60.99	73.15	74.44	76.17	75.43	78.80	78.27	79.24	77.75	80.62	73.94	5.30		
	SRMNet [22]	70.84	69.09	69.51	76.08	75.29	76.46	76.81	73.72	77.53	78.60	78.67	77.66	78.76	80.86	84.73	76.31	4.07		
	RFNet [28]	68.28	55.71	56.04	71.45	69.62	60.33	73.62	71.32	75.24	73.48	73.99	75.94	75.77	70.72	75.92	69.83	6.69		
	mmFormer [29]	81.13	73.15	69.75	87.15	85.26	76.74	88.25	83.21	88.19	88.73	88.71	88.43	89.18	85.81	89.12	84.19	6.05		
	M <sup>2</sup> FTrans [30]	83.49	74.67	73.21	87.45	86.16	78.64	88.28	85.06	88.30	88.46	88.81	88.58	88.93	86.40	89.12	85.04	5.11		
	RMBTS [31]	78.76	75.57	67.98	61.35	77.87	76.11	72.55	73.75	72.19	79.28	80.14	84.40	82.92	80.59	83.56	76.47	6.02		
	RA-HVED [32]	73.33	<b>87.00</b>	71.13	81.29	<b>89.42</b>	<b>87.30</b>	82.85	77.16	84.02	87.55	87.85	84.26	89.23	<b>89.31</b>	88.98	84.05	5.73		
	ACN [34]	82.52	71.80	73.00	87.45	84.28	75.22	88.24	84.27	87.60	87.47	88.21	88.34	87.67	84.37	88.29	83.92	5.61		
	SMUNet [35]	83.75	72.00	76.04	87.67	84.94	77.20	<b>89.35</b>	85.29	88.25	88.14	<b>89.26</b>	<b>89.39</b>	88.31	85.59	89.26	84.96	5.32		
	MSTKDNet [36]	79.81	75.82	<b>78.68</b>	69.19	83.62	80.26	78.66	85.58	75.51	77.05	79.38	83.99	79.73	85.81	84.84	79.86	4.35		
TC	w/o BBDM	81.87	75.63	71.06	86.02	85.03	78.01	87.62	84.20	87.30	88.69	88.39	87.67	88.52	85.65	88.53	84.28	5.19		
	w/o GARM	81.86	74.43	72.49	86.05	83.63	76.39	86.38	82.96	87.76	88.41	88.19	87.26	88.55	84.66	88.25	83.82	5.15		
	w/o LGRM	85.04	79.77	77.45	88.25	86.74	81.34	88.71	86.07	88.95	89.30	89.17	88.95	89.51	86.90	89.45	86.37	3.73		
	<b>Ours</b>	<b>85.21</b>	79.53	76.51	<b>88.45</b>	<b>87.42</b>	81.34	<b>89.69</b>	<b>86.56</b>	<b>89.47</b>	<b>90.59</b>	<b>90.56</b>	<b>89.63</b>	<b>90.73</b>	<b>87.74</b>	<b>90.62</b>	<b>86.94</b>	4.30		
	LCKD [17]	61.97	60.33	66.64	66.16	66.23	68.71	70.65	72.02	71.74	71.62	72.73	73.54	73.37	74.01	74.64	69.62	<b>4.30</b>		
ET	ShaSpec [18]	73.95	45.03	66.21	65.42	76.53	74.90	75.83	75.31	65.60	77.48	80.20	77.12	81.08	79.61	82.79	73.14	9.18		
	MriSeg [19]	59.39	75.37	61.07	32.76	79.48	79.84	61.83	61.69	62.82	74.85	80.16	66.67	79.90	80.43	81.16	69.16	12.76		
	MouseGAN++ [20]	61.92	67.87	60.25	61.79	68.47	60.86	66.28	67.02	67.71	70.33	72.58	67.85	70.97	73.02	74.75	67.44	<u>4.41</u>		
	Hyper-GAE [21]	57.42	62.28	54.38	61.06	72.97	67.42	60.48	61.06	63.09	73.51	79.76	72.58	76.61	80.63	82.42	68.38	8.80		
	SRMNet [22]	62.90	74.62	54.96	61.63	71.95	80.55	67.76	66.03	67.23	71.79	83.20	68.37	72.64	82.65	83.14	71.29	8.19		
	RFNet [28]	53.33	65.47	46.65	55.54	72.07	68.74	59.62	57.83	59.84	73.85	73.90	61.95	75.67	73.08	75.67	64.88	8.92		
	mmFormer [29]	62.76	81.63	59.72	64.00	82.48	81.14	71.64	68.10	69.74	82.58	82.48	72.34	82.66	82.09	82.51	75.06	8.22		
	M <sup>2</sup> FTrans [30]	67.71	82.25	64.82	67.47	83.75	83.46	72.60	72.88	72.67	84.41	84.75	74.26	84.67	84.29	84.67	77.64	7.22		
	RMBTS [31]	61.17	56.77	75.69	44.45	68.19	82.37	78.28	81.92	65.51	63.21	82.71	82.19	68.70	82.83	82.99	71.80	11.45		
	RA-HVED [32]	<b>80.57</b>	64.12	60.31	67.11	81.95	67.42	70.23	81.81	<b>82.20</b>	68.61	70.81	82.99	82.58	82.82	82.93	75.10	7.99		
XLSTM-HVED	XLSTM-HVED [33]	17.08	18.65	50.41	25.89	52.45	55.10	31.36	23.52	55.04	27.45	31.27	60.09	61.50	62.10	62.72	42.31	16.87		
	ACN [34]	69.28	62.80	<u>82.03</u>	68.44	68.69	81.13	<u>83.38</u>	83.24	69.69	69.46	83.32	83.65	70.64	83.11	82.83	76.11	7.39		
	SMUNet [35]	68.98	61.96	81.68	69.91	70.28	82.89	<b>84.25</b>	<u>84.02</u>	71.35	70.95	84.34	<b>84.22</b>	71.69	84.12	84.07	76.98	7.52		
	MSTKDNet [36]	69.28	68.32	<b>83.94</b>	55.34	73.44	84.18	81.92	<b>84.76</b>	61.68	62.83	81.78	<u>83.69</u>	66.95	85.00	83.78	75.13	9.87		
	w/o BBDM	68.45	82.83	64.06	68.78	84.56	83.01	73.39	71.64	73.55	84.53	84.54	74.21	85.25	85.18	84.19	77.88	7.24		
	w/o GARM	70.50	70.39	64.91	68.41	84.97	81.45	71.90	72.29	71.67	84.86	83.79	73.40	85.18	84.36	84.13	77.61	7.02		
	w/o LGRM	72.98	<b>85.65</b>	70.06	<u>74.02</u>	<b>86.26</b>	<b>85.88</b>	76.00	74.51	<u>76.36</u>	<b>86.27</b>	<u>86.33</u>	76.29	<u>86.57</u>	<b>85.87</b>	<u>86.39</u>	<u>80.63</u>	6.08		
	<b>Ours</b>	73.35	85.79	70.98	<b>74.18</b>	<b>86.56</b>	<b>85.92</b>	75.99	74.68	75.57	<b>86.42</b>	<b>86.35</b>	76.47	<b>86.59</b>	<b>86.41</b>	<b>86.94</b>	<b>80.81</b>	6.28		
ET	LCKD [17]	38.36	35.38	46.97	44.73	43.91	48.44	51.73	54.20	<b>52.96</b>	51.89	53.71	55.18	54.35	55.59	56.65	49.60	<b>6.28</b>		
	ShaSpec [18]	30.97	21.24	46.20	25.80	31.29	62.90	53.01	56.71	45.44	62.57	63.05	33.34	61.23	64.26	66.37	48.29	15.36		
	MriSeg [19]	31.34	66.58	35.25	14.88	68.93	68.61	36.30	37.33	34.95	67.35	70.37	39.10	68.99	69.67	70.34	52.00	18.78		
	MouseGAN++ [20]	38.33	41.27	27.28	36.08	41.72	51.38	40.72	41.03	48.91	50.10	58.22	43.25	58.53	56.65	59.46	46.19	9.18		
	Hyper-GAE [21]	34.52	30.72	36.55	38.12	36.79	54.52	48.20	53.11	40.47	52.74	53.36	38.81	53.26	57.50	60.47	45.94	9.33		
	SRMNet [22]	35.19	44.55	26.96	33.24	60.80	58.61	35.91	36.54	39.95	50.55	61.81	38.57	63.15	62.63	63.89	47.49	12.74		
	RFNet [28]	28.13	56.69	17.30	26.53	61.93	59.78	29.44	32.29	33.60	62.32	62.48	35.35	64.47	62.87	64.86	46.54	16.98		
	mmFormer [29]	36.97	68.75	31.48	37.02	70.37	69.46	39.14	43.47	42.57	69.69	69.81	42.29	69.77	70.59	69.82	55.15	15.83		
	M <sup>2</sup> FTrans [30]	40.13	71.18	34.43	35.55	73.19	72.37	41.36	45.63	43.03	72.60	74.85	44.27	74.91	73.46	75.00	58.13	16.62		
	RMBTS [31]	34.66	33.71	46.38	17.35	40.85	50.41	48.31	49.75	37.39	34.82	51.08	59.82	40.74	65.39	64.38	45.00	12.41		
XLSTM-HVED	RA-HVED [32]	39.28	45.62	56.18	<u>46.11</u>	36.65	43.58	43.80	38.44	39.05	44.42	43.49	36.35	36.60	36.24	36.23	41.47	<b>5.33</b>		
	XLSTM-HVED [33]	13.94	14.93	50.98	21.82	53.08	56.37	28.33	19.66	<b>56.81</b>	24.07	28.25	62.11	64.20	64.23	65.55	41.62	19.49		
	ACN [34]	42.25	35.24	69.84	40.27	41.74	70.06	72.06	72.70	42.53	38.42	71.21	71.94	42.75	73.69	71.51	57.08	15.67		
	SMUNet [35]	42.73	34.21	<u>71.21</u>	41.49	42.22	72.38	<u>72.98</u>	74.04	43.59	42.05	72.94	<u>72.53</u>	43.35	72.89	72.49	58.07	15.76		
	MSTKDNet [36]	32.61	40.67	<b>73.82</b>	35.48	41.71	73.09	<b>73.53</b>	<b>74.99</b>	28.72	40.93	73.28	<b>73.85</b>	36.48	75.26	74.07	56.57	18.88		
	w/o BBDM	45.09	75.48	37.09	40.63	<u>76.27</u>	74.75	45.65	46.60	48.65	<u>77.57</u>	<b>77.71</b>	48.34	<u>75.79</u>	<u>75.94</u>	<u>77.25</u>	61.52	16.09		
	w/o GARM	48.16	72.66	35.47	39.33	72.38	74.75	42.74	44.74	45.10	75.08									

Table 6: Quantitative comparison results measured in HD95 (%) on BraTS 2018

Type	Flair	○	○	○	●	○	○	●	○	●	●	●	●	●	○	●	Avg.	Std.
WT	LCKD [17]	9.42	10.62	9.46	8.10	7.69	<b>7.34</b>	6.74	6.67	6.32	6.01	5.72	5.52	5.36	<b>5.31</b>	5.16	7.03	<b>1.66</b>
	ShaSpec [18]	30.29	67.62	74.98	35.17	24.01	17.89	24.43	52.28	26.95	23.77	11.55	21.43	13.67	16.91	10.21	30.08	19.09
	MriSeg [19]	<b>4.00</b>	12.70	<b>9.17</b>	30.53	<b>2.57</b>	<b>4.67</b>	8.12	<b>4.25</b>	<b>3.78</b>	12.70	8.20	<b>3.55</b>	<b>2.46</b>	<b>2.23</b>	<b>2.21</b>	7.41	7.09
	MouseGAN++ [20]	15.51	13.60	14.04	19.14	15.30	16.85	18.71	15.11	16.35	16.54	15.09	14.17	14.82	14.69	9.14	15.27	2.25
XLSTM-HVED	Hyper-GAE [21]	13.63	<b>8.71</b>	16.39	18.48	11.22	9.63	18.85	10.48	11.17	10.32	12.17	10.67	9.64	10.60	8.16	12.01	3.24
	SRMNet [22]	13.90	23.16	20.10	10.87	10.01	14.22	8.20	12.28	7.39	8.29	5.48	7.36	6.62	7.65	7.50	10.87	4.94
	RFNet [28]	38.64	47.90	39.14	34.50	37.47	38.12	27.08	33.85	25.91	29.65	28.56	24.48	23.89	35.36	24.84	32.63	6.75
	mmFormer [29]	12.26	13.78	31.55	9.15	9.45	10.14	7.37	8.20	6.90	7.52	7.29	6.88	5.73	7.13	5.77	9.94	6.18
	M <sup>2</sup> FTrans [30]	9.29	10.60	16.06	8.81	7.29	8.97	6.57	7.73	8.15	8.45	6.18	6.36	8.20	7.03	5.81	8.37	2.42
	RMBTS [31]	13.97	12.43	22.19	39.66	11.35	9.62	20.40	10.74	10.71	8.28	7.72	8.02	7.75	7.14	6.52	13.10	8.38
	RA-HVED	17.02	11.74	23.23	20.21	6.34	11.21	17.04	14.51	14.87	9.80	8.70	14.70	7.74	6.48	7.69	12.75	4.99
	ACN [34]	10.01	13.01	11.60	6.14	8.12	10.59	<b>5.33</b>	8.24	5.39	5.97	<b>5.01</b>	6.00	5.72	7.95	5.99	7.67	2.46
	SMUNet [35]	9.76	12.78	10.92	<b>5.41</b>	7.66	9.49	<b>4.75</b>	6.86	5.33	<b>5.36</b>	<b>4.72</b>	<b>4.83</b>	5.74	6.57	<b>4.77</b>	<b>7.00</b>	2.49
	MSTKDNet [36]	10.77	10.36	<b>9.10</b>	17.49	6.60	8.98	9.05	<b>5.96</b>	16.82	11.12	8.84	7.63	12.42	6.42	7.40	9.93	3.34
TC	w/o BBDM	11.44	9.95	13.59	8.49	7.17	7.99	6.87	7.98	6.89	5.73	5.73	6.97	5.91	7.20	6.51	8.02	2.19
	w/o GARM	9.21	11.14	12.23	8.57	7.81	9.93	6.54	9.00	5.76	5.59	5.80	5.55	7.45	6.04	7.75	2.11	
	w/o LGRM	9.49	9.03	11.06	6.13	7.13	8.53	5.61	7.30	6.68	5.43	5.60	6.42	5.50	6.84	5.30	7.07	1.67
	Ours	<b>6.45</b>	<b>8.26</b>	10.29	<b>5.60</b>	<b>5.96</b>	8.02	6.23	6.51	<b>5.15</b>	<b>5.21</b>	5.25	5.90	<b>5.08</b>	5.93	5.01	<b>6.32</b>	<b>1.42</b>
	LCKD [17]	19.44	16.14	12.50	11.79	12.52	11.08	9.98	9.20	8.99	8.78	8.27	7.90	<b>7.79</b>	7.46	7.20	10.60	3.35
	ShaSpec [18]	36.45	60.32	69.55	45.56	26.04	30.52	25.49	59.48	33.35	37.36	23.00	22.02	24.15	32.86	20.04	36.41	15.00
	MriSeg [19]	12.30	13.79	13.10	32.66	5.26	5.04	12.90	10.14	10.67	12.69	6.09	9.15	5.28	5.27	4.60	10.60	6.78
ET	MouseGAN++ [20]	13.67	13.81	14.69	11.62	9.80	9.58	11.59	11.69	12.62	9.23	10.58	11.03	10.12	9.89	8.25	11.21	<b>1.79</b>
	Hyper-GAE [21]	19.83	21.59	27.28	19.06	17.15	19.83	17.89	19.06	18.10	17.29	14.48	10.07	8.00	8.77	7.80	16.41	5.39
	SRMNet [22]	17.89	22.67	21.27	18.22	12.66	11.44	16.49	14.26	13.94	9.26	8.14	10.12	8.70	7.95	7.40	13.36	4.83
	RFNet [28]	18.43	49.95	31.18	23.73	32.75	42.03	19.04	15.48	16.52	25.61	24.63	13.58	17.87	32.23	17.47	25.37	10.14
	mmFormer [29]	19.71	14.53	30.84	19.25	6.61	13.10	10.84	22.71	10.11	7.23	6.09	15.54	5.50	6.65	5.95	12.98	7.24
	M <sup>2</sup> FTrans [30]	17.08	9.97	25.57	13.10	6.37	6.19	15.43	15.66	8.74	6.09	5.73	8.38	<b>4.53</b>	6.32	4.49	10.24	5.79
	RMBTS [31]	24.56	13.98	27.14	47.79	9.82	6.36	17.08	9.16	12.98	10.94	5.45	6.68	9.83	6.66	5.48	14.26	11.00
	RA-HVED	12.79	17.16	21.89	17.80	7.39	13.91	12.54	11.56	10.03	12.45	10.85	7.53	6.91	6.71	6.68	11.75	4.40
	XLSTM-HVED	109.16	109.43	89.07	99.65	91.95	85.00	84.12	103.91	88.24	98.96	83.67	70.80	72.37	72.82	68.53	88.51	13.22
	ACN [34]	10.95	12.95	<b>7.62</b>	11.36	10.92	8.01	<b>5.55</b>	5.34	10.99	11.42	5.16	<b>5.09</b>	10.83	5.44	5.48	8.47	2.84
MSTKDNet [36]	SMUNet [35]	11.67	12.31	8.63	10.59	10.56	6.23	<b>5.09</b>	<b>5.33</b>	10.47	10.67	<b>4.99</b>	<b>5.04</b>	10.65	5.20	5.03	8.16	2.81
	w/o BBDM	10.79	16.12	<b>6.42</b>	21.77	8.49	5.19	6.00	<b>4.97</b>	19.98	18.28	6.15	5.72	11.23	5.35	5.80	10.15	5.76
	w/o GARM	10.19	6.25	11.98	11.11	5.07	7.07	8.87	9.23	8.76	5.31	5.03	8.09	5.09	5.13	5.19	7.49	2.35
	w/o LGRM	9.88	7.73	12.73	11.32	5.29	7.21	9.70	10.79	9.10	5.42	5.07	8.40	4.99	5.53	5.35	7.90	2.51
	Ours	<b>8.80</b>	<b>4.78</b>	10.57	<b>9.98</b>	<b>4.82</b>	<b>4.92</b>	7.68	7.90	<b>8.58</b>	<b>4.72</b>	5.03	7.81	4.85	<b>4.87</b>	<b>4.47</b>	<b>6.65</b>	<b>2.10</b>
	LCKD [17]	50.79	54.74	48.82	47.27	48.82	46.86	45.23	44.01	<b>43.69</b>	44.04	43.27	42.65	42.95	42.51	42.07	45.85	<b>3.53</b>
	ShaSpec [18]	57.54	74.89	65.64	54.05	53.23	48.57	51.70	69.00	51.29	47.63	42.09	48.22	40.41	43.30	38.73	52.42	10.21
	MriSeg [19]	45.90	42.78	47.01	64.44	36.79	36.49	46.87	43.83	45.03	41.45	38.00	43.07	36.31	36.69	35.93	42.71	7.05
ET	MouseGAN++ [20]	97.54	98.70	97.92	87.46	80.73	89.93	93.44	84.26	93.73	88.77	87.89	80.09	77.21	76.85	68.65	86.88	8.55
	Hyper-GAE [21]	107.79	109.44	93.89	99.23	96.76	87.79	87.95	99.25	88.73	97.36	76.60	77.38	75.17	75.70	73.04	89.74	11.66
	SRMNet [22]	108.89	99.33	101.64	98.62	89.63	90.92	90.68	96.47	85.27	78.55	68.31	66.15	66.50	67.61	64.65	84.88	14.59
	RFNet [28]	50.67	76.68	55.02	52.13	62.38	68.48	54.89	46.30	45.56	45.79	54.62	48.37	47.90	61.27	47.16	55.27	8.56
	mmFormer [29]	81.11	44.76	70.48	44.48	36.58	49.50	43.94	80.14	55.51	36.91	37.03	62.16	36.74	37.51	37.03	50.26	15.47
	M <sup>2</sup> FTrans [30]	62.48	37.08	64.16	76.07	36.42	<b>35.93</b>	74.95	60.49	79.16	36.36	<b>29.61</b>	56.98	<b>29.30</b>	36.25	<b>29.24</b>	49.63	18.01
	RMBTS [31]	103.70	121.46	95.57	104.91	102.45	96.74	99.07	116.84	83.46	98.03	86.70	76.84	72.56	76.68	66.72	93.45	15.43
	RA-HVED	71.22	40.49	<b>33.34</b>	<b>43.51</b>	72.42	42.33	44.21	71.65	72.35	45.46	46.56	72.48	72.58	72.72	72.95	58.28	15.24
	XLSTM-HVED	112.03	111.66	91.51	103.45	94.23	84.43	84.34	104.04	85.39	99.16	83.71	67.96	69.32	69.84	65.41	88.43	15.16
	ACN [34]	43.99	45.44	38.52	44.89	43.63	38.18	36.52	36.33	43.96	44.94	36.22	36.15	43.91	<b>29.85</b>	36.62	39.94	<b>4.56</b>
MSTKDNet [36]	SMUNet [35]	43.80	51.78	38.21	44.02	43.77	42.24	<b>36.10</b>	<b>30.17</b>	43.81	43.94	36.23	<b>36.12</b>	43.82	36.66	36.36	40.47	5.16
	w/o BBDM	44.25	61.77	<b>31.17</b>	46.97	49.63	36.54	<b>30.96</b>	<b>29.67</b>	51.05	50.12	30.95	<b>30.65</b>	56.02	30.25	30.79	40.72	10.75
	w/o GARM	65.52	<b>35.43</b>	69.25	61.42	42.02	42.07	78.56	58.84	47.91	48.55	42.16	65.70	<b>35.52</b>	35.52	35.58	50.94	13.91
	w/o LGRM	<b>35.98</b>	44.40	75.32	68.88	49.42	37.13	74.03	61.71	48.83	35.93	35.68	59.98	36.17	42.94	42.66	49.94	13.92
	Ours	41.86	36.06	44.70	44.69	<b>35.74</b>	36.85	48.53	41.43	<b>41.04</b>	<b>28.87</b>	<b>22.63</b>	47.45	35.53	36.01	<b>29.23</b>	<b>38.04</b>	7.04

Table 7: Quantitative comparison results measured in IoU (%) on BraTS 2018

Type		Flair	○	○	○	●	○	○	●	○	●	●	●	●	●	○	●		Avg.	Std.
WT	LCKD [17]	66.33	61.06	60.35	64.55	65.70	65.20	67.38	67.88	69.15	70.19	71.17	71.96	72.55	72.56	73.09	67.94	3.95		
	ShaSpec [18]	66.93	29.31	30.29	52.96	70.62	70.82	71.34	41.69	56.37	58.10	72.11	72.82	73.10	59.76	73.94	60.01	14.85		
	MriSeg [19]	72.00	54.50	66.30	33.65	75.93	70.94	69.63	76.00	75.77	51.43	68.71	77.13	78.97	78.87	78.57	68.56	12.34		
	MouseGAN++ [20]	68.27	60.95	54.48	67.45	64.88	57.01	65.68	62.28	66.52	67.22	69.41	69.38	68.44	67.01	70.27	65.28	4.50		
XLSTM-HVED	Hyper-GAE [21]	60.83	62.68	<b>66.84</b>	63.35	67.07	70.83	65.90	63.44	61.00	63.03	64.13	69.99	69.89	68.59	71.31	65.92	<b>3.46</b>		
	SRMNet [22]	69.59	55.27	55.53	66.58	65.22	63.14	67.58	73.33	68.57	70.11	70.25	73.88	75.39	76.09	75.39	68.39	6.32		
	RFNet [28]	53.99	40.78	41.47	57.85	55.28	45.48	60.33	57.27	62.25	60.17	60.72	63.09	62.86	56.52	63.05	56.07	7.34		
	mmFormer [29]	50.97	<u>72.69</u>	47.53	50.63	73.77	<u>72.36</u>	59.07	56.19	57.55	73.72	73.88	60.20	74.05	73.40	73.98	64.67	9.92		
	M <sup>2</sup> FTrans [30]	72.68	61.94	60.54	78.35	76.40	66.28	79.65	74.85	79.65	79.87	80.45	80.12	80.62	76.79	80.93	75.27	6.66		
	RMBTS [31]	67.51	65.75	54.64	48.08	69.02	69.48	59.92	66.42	61.69	68.28	69.67	70.43	69.19	70.25	73.30	65.58	6.57		
	RA-HVED [32]	60.08	<b>77.75</b>	56.98	69.97	<b>81.32</b>	<b>78.20</b>	72.02	64.15	73.49	78.72	79.14	73.73	<u>81.11</u>	<b>81.15</b>	80.74	73.90	7.67		
	ACN [34]	50.11	67.66	41.34	50.79	57.27	71.64	72.08	71.04	52.93	58.90	73.11	73.48	73.88	61.15	74.29	63.37	10.43		
	SMUNet [35]	71.70	58.71	59.96	78.67	74.03	62.24	79.53	73.73	78.83	78.68	79.50	79.73	78.89	73.97	79.69	73.86	7.26		
	MSTKDNet [36]	67.82	63.31	66.32	56.97	72.82	68.11	66.61	75.46	63.79	65.61	67.55	73.61	69.27	75.77	74.80	68.52	5.08		
TC	w/o BBDM	70.92	62.77	57.28	76.31	75.05	65.34	78.63	73.90	78.18	80.28	79.87	78.81	80.09	75.94	80.10	74.23	6.88		
	w/o GARM	71.11	61.38	59.07	76.64	73.09	63.30	77.15	72.66	78.93	79.91	76.62	78.36	80.12	74.61	79.72	73.71	6.85		
	w/o LGRM	73.08	65.43	62.04	77.44	76.00	67.34	79.30	74.92	79.11	80.77	80.68	79.27	80.93	76.51	80.84	75.58	5.86		
	Ours	<b>75.07</b>	67.78	65.07	<b>79.69</b>	<u>77.37</u>	69.43	<u>80.33</u>	<b>76.49</b>	<b>80.68</b>	<b>81.22</b>	<u>81.05</u>	<u>80.68</u>	<b>81.53</b>	<u>77.61</u>	<b>81.43</b>	<b>77.03</b>	5.22		
	LCKD [17]	49.94	48.09	55.81	54.88	54.86	57.94	60.30	61.97	61.46	61.18	62.55	63.57	63.26	64.07	64.84	58.98	<b>5.03</b>		
	ShaSpec [18]	39.95	22.64	38.99	38.14	44.42	58.39	45.82	51.17	38.91	58.68	63.07	47.07	63.02	61.23	64.24	49.05	11.82		
	MriSeg [19]	45.01	65.35	47.21	21.36	69.35	69.55	48.51	47.77	48.74	64.69	70.38	52.50	69.92	70.45	71.43	57.48	13.97		
	MouseGAN++ [20]	49.96	69.00	47.00	46.48	71.06	70.26	57.46	53.62	52.57	67.90	71.32	51.95	72.64	73.18	73.39	61.85	10.26		
ET	Hyper-GAE [21]	0.44	0.47	0.46	0.49	0.65	0.64	0.59	0.59	0.57	0.57	0.60	0.53	0.66	0.59	0.66	0.57	<b>0.07</b>		
	SRMNet [22]	49.20	66.26	40.32	46.80	72.72	71.72	53.54	52.27	53.30	72.64	74.38	54.69	73.37	73.55	74.13	61.93	11.73		
	RFNet [28]	40.79	53.40	34.13	41.39	60.73	56.88	46.12	45.14	46.71	62.30	62.41	49.04	64.58	61.89	64.52	52.67	9.66		
	mmFormer [29]	50.97	72.69	47.53	50.63	73.77	72.36	59.07	56.19	57.55	73.72	73.88	60.20	74.05	73.40	73.98	64.67	9.92		
	M <sup>2</sup> FTrans [30]	55.78	74.04	52.36	54.56	75.60	74.95	60.59	60.69	60.58	75.99	76.41	62.59	76.42	76.01	76.41	67.53	9.12		
	RMBTS [31]	47.52	42.77	66.06	32.20	54.72	73.35	69.17	72.82	52.01	50.02	74.12	73.25	55.68	73.86	74.29	60.79	13.32		
	RA-HVED [32]	<b>71.14</b>	50.47	46.31	53.68	72.90	54.19	57.09	72.35	<b>72.76</b>	55.58	58.12	73.92	73.42	73.84	73.94	63.98	10.04		
	XLSTM-HVED [33]	10.89	12.57	41.27	18.39	43.50	46.09	23.71	16.13	46.21	19.61	23.60	51.25	52.83	53.47	54.04	34.24	16.02		
	ACN [34]	56.41	48.92	<u>73.23</u>	54.95	55.65	72.75	<b>74.51</b>	74.45	56.35	56.09	74.59	<u>74.82</u>	57.34	74.27	74.08	65.23	9.65		
	SMUNet [35]	55.52	48.63	72.82	56.32	57.12	74.61	<b>75.26</b>	<u>75.01</u>	57.92	57.38	75.65	<b>75.40</b>	58.34	75.34	75.59	66.06	9.77		
ET	MSTKDNet [36]	55.76	55.05	<b>75.21</b>	43.77	60.56	75.50	72.62	<b>76.38</b>	48.59	50.28	72.34	74.69	54.09	76.64	74.75	64.42	11.65		
	w/o BBDM	55.91	74.46	51.31	55.45	76.13	74.48	61.03	58.95	60.90	76.26	76.55	61.51	<u>77.05</u>	<u>76.83</u>	76.15	67.53	9.38		
	w/o GARM	57.78	73.73	51.31	54.78	76.40	72.59	59.01	59.34	58.60	76.35	75.04	60.48	76.73	75.58	75.41	66.88	9.21		
	w/o LGRM	59.52	<u>75.75</u>	56.90	<u>59.13</u>	<u>76.93</u>	<u>75.95</u>	62.45	60.99	62.05	<u>77.10</u>	<u>76.86</u>	62.91	<u>77.05</u>	76.73	<u>77.56</u>	<u>69.19</u>	8.20		
	Ours	<u>60.62</u>	<b>77.55</b>	57.42	<b>61.47</b>	<b>78.15</b>	<b>77.60</b>	63.81	62.32	<u>64.43</u>	<b>78.30</b>	<b>78.37</b>	64.22	<b>78.56</b>	<b>77.71</b>	<b>78.41</b>	<b>70.60</b>	8.16		
	LCKD [17]	27.97	24.94	36.91	<u>34.55</u>	33.56	38.22	41.59	44.13	42.76	41.61	43.49	45.01	44.10	45.39	46.49	39.38	<b>6.35</b>		
ET	ShaSpec [18]	19.84	6.48	34.51	16.22	20.01	50.78	21.41	44.53	15.97	50.72	53.00	21.61	52.31	52.23	53.26	34.19	16.69		
	MriSeg [19]	20.45	56.27	23.53	8.97	57.96	57.72	24.66	25.42	23.47	57.08	59.69	26.87	58.37	58.88	59.54	41.26	18.52		
	MouseGAN++ [20]	28.48	31.22	27.15	<b>35.53</b>	43.24	40.37	41.16	42.13	41.34	43.92	41.87	45.54	39.37	53.54	54.81	40.64	<u>7.57</u>		
	Hyper-GAE [21]	26.97	51.16	22.82	19.84	46.43	46.97	30.37	39.84	37.22	50.82	51.24	43.26	53.40	55.56	56.16	42.14	11.70		
	SRMNet [22]	23.83	54.59	16.97	22.01	60.10	58.40	24.34	25.23	27.80	59.86	61.21	26.92	50.49	61.04	61.33	42.27	17.57		
	RFNet [28]	18.83	45.14	10.59	17.54	50.28	48.03	19.83	22.31	23.38	50.56	50.65	24.97	52.80	51.13	53.24	35.95	15.66		
	mmFormer [29]	26.74	58.59	21.65	26.27	59.83	59.26	28.22	28.98	31.21	59.08	59.21	31.43	59.14	59.93	59.13	44.58	15.85		
	M <sup>2</sup> FTrans [30]	29.40	61.39	24.67	25.69	63.22	62.29	30.42	34.33	31.91	62.49	64.78	33.17	64.87	63.43	64.98	47.80	16.89		
	RMBTS [31]	23.31	22.51	58.43	10.38	28.53	60.24	58.52	59.67	25.75	24.04	60.83	59.85	28.84	60.99	61.09	42.87	18.70		
	RA-HVED [32]	<b>60.87</b>	28.44	22.27	30.90	62.07	30.08	31.81	61.11	<b>61.78</b>	32.87	33.96	<u>61.98</u>	62.13	62.40	62.59	47.02	16.07		
ET	XLSTM-HVED [33]	8.31	9.58	41.95	14.70	44.28	47.55	20.94	12.81	<u>48.23</u>	16.54	20.85	53.52	55.84	55.90	57.33	33.89	18.55		
	ACN [34]	29.79	23.37	59.60	28.07	29.24	59.82	61.57	61.65	30.01	26.53	60.75	61.20	30.18	62.88	60.77	45.70	16.48		
	SMUNet [35]	30.12	22.98	<u>60.94</u>	29.22	29.65	62.03	<b>62.61</b>	<u>63.48</u>	30.95	29.65	62.45	<u>61.98</u>	30.77	62.19	61.84	46.72	16.63		
	MSTKDNet [36]	21.97	29.00	<b>62.39</b>	25.57	30.20	62.49	<u>62.50</u>	<b>64.65</b>	19.11	29.99	62.38	<b>63.43</b>	25.55	64.80	63.35	45.83	18.83		
	w/o BBDM	32.76	65.67	25.64	28.91	<b>66.43</b>	64.74	33.96	34.22	35.84	<b>67.87</b>	<b>67.66</b>	35.82	<u>66.00</u>	<u>66.14</u>	<u>67.14</u>	50.59	17.15		
	w/o GARM	35.31	62.93	24.70	28.31	62.75	64.73	31.61	32.47	32.50	65.45	<u>66.38</u>	34.97	64.68	64.39	64.60	49.05	16.69		
	w/o LGRM	36.88	<u>65.96</u>	30.94	33.15	64.39	<b>65.94</b>	36.92	36.05	37.94	<u>65.80</u>	65.32</								

Table 8: Quantitative comparison results measured in Sensitivity (%) on BraTS 2018

Type	Flair	○	○	○	●	○	○	●	○	●	●	●	●	○	●	Avg.	Std.	
WT	LCKD [17]	75.22	71.97	71.48	75.23	75.85	75.52	77.34	77.59	78.65	79.60	80.42	81.03	81.49	81.40	81.76	77.64	3.26
	ShaSpec [18]	74.92	46.81	57.55	68.16	76.31	77.60	74.86	63.17	67.09	72.71	76.99	74.39	76.38	71.86	75.48	70.29	8.35
	MriSeg [19]	71.48	68.62	69.94	65.10	71.42	70.33	69.76	71.34	70.88	69.69	70.84	71.16	70.19	70.82	71.07	70.18	1.56
	MouseGAN++ [20]	70.99	69.47	65.44	65.94	68.31	68.72	64.10	70.84	69.33	69.52	69.94	70.82	68.36	67.30	70.23	68.62	2.02
XLSTM-HVED	Hyper-GAE [21]	68.79	64.11	67.83	68.18	68.38	67.79	60.38	69.18	68.15	68.61	68.60	70.07	70.81	67.66	72.03	68.01	2.64
	SRMNet [22]	66.49	68.54	69.94	70.15	77.00	72.07	71.00	47.44	70.76	76.08	74.05	79.66	80.43	80.95	82.66	74.28	4.83
	RFNet [28]	70.83	69.99	68.55	71.85	71.20	70.11	71.96	70.92	71.74	72.06	72.03	71.76	71.89	71.25	71.89	71.20	<b>0.96</b>
	mmFormer [29]	68.89	67.92	67.01	70.84	69.77	68.57	70.98	69.30	70.95	71.00	71.01	70.96	70.97	69.89	70.94	69.93	1.27
	M <sup>2</sup> FTrans [30]	69.79	68.24	68.00	71.03	70.23	68.95	71.15	70.07	71.03	71.25	71.18	71.07	71.16	70.35	71.14	70.31	<b>1.07</b>
	RMBTS [31]	70.77	75.03	72.12	66.68	78.36	78.19	72.65	72.88	72.34	66.16	77.41	73.64	77.67	75.60	79.95	73.96	3.96
	RA-HVED [32]	71.76	<b>91.71</b>	73.85	82.89	<b>91.41</b>	<b>92.94</b>	84.78	76.22	84.18	<b>91.86</b>	<b>91.90</b>	85.55	<b>92.00</b>	<b>92.08</b>	<b>92.30</b>	86.36	7.07
	ACN [34]	66.91	69.23	64.80	66.03	67.52	69.66	69.05	69.99	65.89	67.73	69.57	69.52	69.64	66.75	69.91	68.15	1.67
	SMUNet [35]	81.98	72.13	77.05	88.00	84.40	77.38	<b>91.24</b>	83.97	88.56	88.85	90.95	<b>90.70</b>	89.21	83.09	89.91	85.16	5.69
	MSTKDNet [36]	83.04	70.58	77.18	87.32	83.50	75.76	89.56	83.35	88.46	88.79	88.90	88.65	88.24	83.36	88.87	84.37	5.58
TC	w/o BBDM	<b>88.67</b>	82.11	77.79	89.44	89.33	82.63	90.37	<b>89.67</b>	<b>90.42</b>	<b>91.77</b>	<b>91.67</b>	90.31	91.53	89.53	91.77	88.47	4.04
	w/o GARM	88.35	81.27	79.04	86.40	<b>91.37</b>	84.75	86.44	89.54	89.02	89.98	90.11	90.26	91.99	89.99	90.74	87.95	3.62
	w/o LGRM	86.83	79.96	<b>81.88</b>	89.55	89.64	82.11	89.99	<b>90.40</b>	90.07	91.41	91.54	90.20	<b>92.17</b>	90.13	92.03	88.53	3.83
	Ours	<b>89.10</b>	<b>83.74</b>	<b>81.85</b>	<b>90.29</b>	90.76	<b>84.95</b>	<b>90.52</b>	89.02	<b>91.51</b>	91.14	91.09	<b>91.54</b>	91.31	<b>90.53</b>	91.51	<b>89.26</b>	3.02
	LCKD [17]	67.07	66.68	71.72	72.28	72.13	73.87	75.46	76.54	76.45	76.70	77.63	78.22	78.07	78.46	78.91	74.68	3.83
ET	ShaSpec [18]	73.95	45.03	66.21	65.42	76.53	74.90	75.83	75.31	65.60	77.48	80.20	77.12	81.08	79.61	82.79	73.14	9.18
	MriSeg [19]	64.65	68.48	66.43	60.82	70.19	69.39	65.99	64.38	66.20	69.07	70.31	66.70	68.86	69.02	69.55	67.34	2.56
	MouseGAN++ [20]	69.49	68.08	64.56	64.69	66.09	67.64	63.40	70.36	68.90	69.69	70.79	70.96	67.30	68.34	69.91	68.01	<b>2.31</b>
	Hyper-GAE [21]	64.29	67.40	64.11	65.41	67.92	67.29	63.54	65.41	65.37	68.31	69.10	68.90	72.80	67.47	72.94	67.35	2.75
	SRMNet [22]	67.83	68.47	60.80	61.02	73.59	78.63	68.29	65.20	66.82	73.53	74.29	66.43	74.05	82.68	83.77	71.03	6.78
	RFNet [28]	62.44	69.41	61.67	64.54	69.39	69.50	65.89	64.05	64.81	70.00	69.95	65.74	69.85	69.45	69.85	67.10	2.93
	mmFormer [29]	64.65	68.48	66.43	60.82	70.19	69.39	65.99	64.38	66.20	69.07	70.31	66.70	68.86	69.02	69.55	67.34	2.56
	M <sup>2</sup> FTrans [30]	66.54	69.26	65.89	66.64	69.36	69.49	67.91	68.00	67.78	69.87	70.05	68.48	69.72	69.58	69.85	68.56	<b>1.32</b>
	RMBTS [31]	66.94	53.86	78.38	41.82	69.94	82.71	78.18	84.00	70.05	62.94	82.57	83.66	70.55	84.03	83.69	72.89	12.15
	RA-HVED [32]	<b>87.06</b>	<b>88.44</b>	79.92	<b>87.70</b>	<b>89.51</b>	<b>89.66</b>	87.73	<b>87.55</b>	<b>90.04</b>	<b>90.33</b>	<b>90.41</b>	<b>89.48</b>	<b>90.65</b>	<b>90.18</b>	<b>90.53</b>	<b>88.61</b>	2.61
XLSTM-HVED	XLSTM-HVED [33]	68.98	66.54	73.42	69.34	74.72	74.28	68.69	68.52	75.16	69.99	68.65	74.31	75.57	74.68	75.16	71.87	3.10
	ACN [34]	73.33	67.52	<b>86.43</b>	74.94	73.03	85.46	<b>90.29</b>	86.75	77.64	78.17	<b>89.04</b>	<b>89.20</b>	78.10	85.56	87.04	81.50	6.94
	SMUNet [35]	74.79	64.69	<b>86.08</b>	75.43	74.84	85.67	<b>89.06</b>	<b>88.39</b>	78.09	78.12	88.13	88.09	77.92	87.58	87.26	81.61	7.05
	MSTKDNet [36]	74.01	65.95	83.48	49.65	78.30	83.82	79.64	87.44	60.03	59.80	79.38	83.72	66.61	87.55	83.87	74.88	11.31
	w/o BBDM	<b>80.12</b>	<b>87.49</b>	75.62	<b>78.52</b>	<b>87.96</b>	<b>87.63</b>	80.30	81.51	<b>81.87</b>	<b>87.87</b>	87.49	81.14	<b>87.81</b>	<b>88.42</b>	<b>88.92</b>	<b>84.18</b>	4.27
ET	w/o GARM	76.31	82.99	69.56	74.86	86.19	82.27	74.09	75.26	80.26	85.88	84.12	78.70	87.47	86.48	85.20	80.64	5.36
	w/o LGRM	78.43	84.90	76.23	75.75	87.78	86.22	76.15	80.32	80.03	86.35	88.16	80.40	87.03	88.41	87.06	82.88	4.66
	Ours	78.57	86.69	77.00	78.23	87.80	87.53	78.89	79.57	81.17	86.85	87.18	80.56	<b>88.28</b>	87.09	88.54	83.60	4.29
	LCKD [17]	55.17	52.32	61.68	61.42	60.54	63.68	66.06	67.94	67.37	67.01	68.33	69.44	69.02	69.85	70.62	64.70	5.31
	ShaSpec [18]	58.42	20.68	68.14	36.39	52.29	76.86	53.30	71.52	38.17	74.17	76.76	53.54	77.56	73.93	77.57	60.62	17.32
Ours	MriSeg [19]	62.67	70.23	64.49	59.45	70.76	70.25	63.97	63.26	64.39	70.71	71.27	64.28	69.72	70.37	70.63	67.10	3.82
	MouseGAN++ [20]	63.63	67.53	65.95	63.48	65.94	65.81	64.93	67.00	64.72	65.02	65.50	66.06	65.15	65.85	68.74	65.69	<b>1.32</b>
	Hyper-GAE [21]	63.57	64.93	62.83	62.04	66.02	66.57	64.15	65.04	61.95	67.76	68.39	63.95	69.59	69.36	69.92	65.74	<b>2.65</b>
	SRMNet [22]	47.98	77.88	37.85	44.11	80.18	77.85	46.40	45.00	51.16	81.26	81.61	47.85	81.27	78.59	81.15	64.01	17.31
	RFNet [28]	61.21	71.23	58.09	61.22	71.17	71.15	62.65	62.62	63.41	71.29	71.36	64.22	71.32	71.13	71.31	66.89	4.82
	mmFormer [29]	63.70	70.62	62.89	62.96	70.73	70.83	64.44	64.44	65.04	70.58	70.61	65.23	70.59	70.73	70.65	67.60	3.33
	M <sup>2</sup> FTrans [30]	64.81	70.76	62.81	62.93	71.14	71.10	64.89	65.38	65.40	71.13	71.30	65.76	71.22	71.23	71.28	68.08	3.37
	RMBTS [31]	39.11	34.41	65.38	14.71	46.11	68.05	65.72	67.08	39.75	36.51	68.39	67.15	44.00	69.24	68.79	52.96	16.87
	RA-HVED [32]	<b>84.70</b>	<b>84.30</b>	56.34	<b>77.39</b>	<b>85.33</b>	75.66	70.56	<b>82.73</b>	<b>86.21</b>	<b>84.78</b>	80.84	<b>84.04</b>	<b>86.06</b>	<b>84.24</b>	<b>84.59</b>	<b>80.52</b>	7.75
	XLSTM-HVED [33]	<b>67.59</b>	66.00	74.11	68.29	75.34	74.95	68.16	67.42	<b>75.78</b>	68.91	67.90	74.90	76.16	75.25	75.83	<b>71.77</b>	3.83
Ours	ACN [34]	61.04	49.60	80.17	59.89	57.61	79.00	<b>81.73</b>	80.60	64.59	53.21	79.60	81.44	60.57	79.54	80.39	69.93	11.57
	SMUNet [35]	63.70	46.96	<b>81.36</b>	62.25	57.84	82.04	<b>82.37</b>	81.94	64.42	60.95	82.71	<b>82.89</b>	59.94	81.38	81.65	71.49	11.89
	MSTKDNet [36]	41.90	48.88	<b>81.18</b>	41.73	49.71	80.65	79.02	<b>82.43</b>	37.42	48.84	78.09	81.06	46.18	<b>83.03</b>	81.08	64.08	18.17
	w/o BBDM	46.49	81.53	44.89	41.60	<b>82.02</b>	<b>83.59</b>	47.83	49.34	49.49	<b>83.93</b>	<b>85.02</b>	50.84	<b>82.46</b>	82.07	81.67	66.18	17.88
	w/o GARM	48.62	79.14	52.59	51.47	78.11	82.54	59.44	51.01	51.22	83.16	<b>82.97</b>	55.58	79.81	81.68	80.84	67.88	14.30
Ours	w/o LGRM	53.80	77.30	46.57	46.76	75.45	78.39</											

#### 4.5.1. *Ablation of the Bi-Bottleneck Distillation Module*

When BBDM including the GSME feature-distillation branch and the teacher-student discriminator was removed, the Dice scores for ET, WT, and TC fell by 5.16%, 3.01%, and 2.82%, respectively, while HD95 rose to 3.72 mm, 2.71 mm, and 2.05 mm; Sensitivity and IoU likewise declined markedly. Without GSME, the student model loses structural-textural alignment guidance and cannot exploit the priors of complete modalities to compensate for missing information. Eliminating the discriminator removes style regularization, causing shallow features to drift over time and the decoder to miss fine textures, thereby leading to fragmented or jagged boundaries. The absence of adversarial regularization also weakens robustness to input noise and modality perturbations. These results underscore BBDM’s central role in facilitating knowledge transfer and maintaining resilience.

#### 4.5.2. *Ablation of the Graph-guided Adaptive Refinement Module*

Removing GARM reduced the Dice scores for ET, WT, and TC by 5.01%, 3.53%, and 3.25%, with HD95 increasing to 3.00 mm, 7.71 mm, and 7.03 mm; Sensitivity and IoU dropped in parallel. Without the modality-combination residuals (CF) from the Adapter Bank and their graph-based alignment with general features (GF), the model’s ability to adapt to different missing-modality combinations weakens. Structural guidance is lost, breaking connectivity in internal regions (e.g., necrotic core, enhancing zones) and diminishing deformation recovery. During sliding-window refinement the coarse mask cannot adjust to modality-specific contrast and texture, causing edge collapse and more false positives, which harms both Sensitivity and IoU. These findings confirm GARM as a key module for structural recovery and cross-combination robustness.

#### 4.5.3. *Ablation of the Lesion-presence Guided Reliability Module*

Removing LGRM substantially lowered Dice for ET, WT, and TC by 3.77%, 5.12%, and 6.02% and raised HD95 to 3.19 mm, 26.94 mm, and 31.29 mm; Sensitivity and IoU deteriorated accordingly. Without lesion-presence probability guidance, pronounced boundary shifts arise during ROI cropping and sliding-window stitching; low-contrast areas and vascular artifacts are frequently misclassified as lesions, thereby markedly increasing false positives. Uncertain regions lack BCE feedback, yielding blurred masks, missing ET details, and disjoint WT envelopes, which impair 3D visualization and volume estimation. Thus, LGRM not only boosts aggregate performance as

an auxiliary branch but also supplies dynamic reliability constraints essential for accuracy and cross-domain robustness.

## 5. Conclusion

This paper proposes AdaMM, a multi-modal brain tumor segmentation framework designed for missing-modality scenarios, addressing the robustness and generalization challenges caused by incomplete MRI inputs in clinical settings. Centered on knowledge distillation, AdaMM integrates three complementary modules: GARM explicitly models semantic associations between general and modality-specific features to improve adaptability; BBDM enables precise bottleneck feature transfer between teacher and student networks via style alignment and adversarial learning; and LGRM incorporates lesion-aware priors through an auxiliary classification task to suppress false positives under missing modalities. To comprehensively evaluate performance, we construct a brain tumor segmentation benchmark for missing-modality scenarios using the BraTS 2018 and 2024 datasets, and systematically compare six major categories of existing methods. Experimental results demonstrate that AdaMM consistently outperforms state-of-the-art approaches under both complete and incomplete modality settings, validating the effectiveness of its design and offering practical guidance for algorithm selection and future research. This work contributes a robust and generalizable solution for multi-modal medical image segmentation under incomplete inputs. Future directions include integrating self-supervised learning, extending to other organs and tasks, and enabling efficient deployment in resource-limited or time-constrained clinical environments.

## CRediT authorship contribution statement

**Shenghao Zhu:** Methodology, Visualization, Writing – original draft. **Yifei Chen:** Conceptualization, Methodology, Writing – original draft. **Weihong Chen:** Validation, Visualization. **Shuo Jiang:** Validation, Visualization. **Guanyu Zhou:** Validation, Visualization. **Yuanhan Wang:** Validation, Visualization. **Feiwei Qin:** Supervision, Writing – review & editing. **Changmiao Wang:** Writing – review & editing. **Qiyuan Tian:** Project administration, Writing – review & editing.

## Declaration of competing interest

The authors declare that they have no known competing financial interests or personal relationships that could have appeared to influence the work reported in this paper.

## Acknowledgments

This work was supported by the National Natural Science Foundation of China (No. 82302166), Tsinghua University Startup Fund, Fundamental Research Funds for the Provincial Universities of Zhejiang (No. GK259909299001-006), Anhui Provincial Joint Construction Key Laboratory of Intelligent Education Equipment and Technology (No. IEET202401), and Guangdong Basic and Applied Basic Research Foundation (No. 2025A1515011617).

## References

- [1] M. Havaei, A. Davy, D. Warde-Farley, A. Biard, A. Courville, Y. Bengio, C. Pal, P.-M. Jodoin, H. Larochelle, Brain tumor segmentation with deep neural networks, *Medical Image Analysis* 35 (2017) 18–31.
- [2] D. Verhaert, P. Thavendiranathan, S. Giri, G. Mihai, S. Rajagopalan, O. P. Simonetti, S. V. Raman, Direct T2 quantification of myocardial edema in acute ischemic injury, *JACC: Cardiovascular Imaging* 4 (2011) 269–278.
- [3] J. N. Sarkaria, L. S. Hu, I. F. Parney, D. H. Pafundi, D. H. Brinkmann, N. N. Laack, C. Giannini, T. C. Burns, S. H. Kizilbash, J. K. Laramy, et al., Is the blood–brain barrier really disrupted in all glioblastomas? A critical assessment of existing clinical data, *Neuro-oncology* 20 (2018) 184–191.
- [4] S. Bauer, R. Wiest, L.-P. Nolte, M. Reyes, A survey of MRI-based medical image analysis for brain tumor studies, *Physics in Medicine & Biology* 58 (2013) R97.
- [5] C. He, Y. Shen, C. Fang, F. Xiao, L. Tang, Y. Zhang, W. Zuo, Z. Guo, X. Li, Diffusion models in low-level vision: A survey, *IEEE Transactions on Pattern Analysis and Machine Intelligence* 47 (2025) 4630–4651.

[6] C. Lu, J. Zhang, D. Zhang, L. Mou, J. Yuan, K. Xia, Z. Guo, J. Zhang, Fine-Grained hierarchical progressive modal-aware network for brain tumor segmentation, *IEEE Journal of Biomedical and Health Informatics* (2025) 1–13.

[7] S. Wang, Y. Lin, Y. Wu, B. Du, Toward real ultra image segmentation: Leveraging surrounding context to cultivate general segmentation model, in: *Advances in Neural Information Processing Systems*, volume 37, 2024, pp. 129227–129249.

[8] Y. Chen, B. Zou, Z. Guo, Y. Huang, Y. Huang, F. Qin, Q. Li, C. Wang, SCUNet++: Swin-UNet and CNN bottleneck hybrid architecture with multi-fusion dense skip connection for pulmonary embolism CT image segmentation, in: *Proceedings of the IEEE/CVF Winter Conference on Applications of Computer Vision*, 2024, pp. 7759–7767.

[9] C. Zhang, Y. Chen, Z. Fan, Y. Huang, W. Weng, R. Ge, D. Zeng, C. Wang, TC-DiffRecon: Texture coordination MRI reconstruction method based on diffusion model and modified MF-UNet method, in: *IEEE International Symposium on Biomedical Imaging*, 2024, pp. 1–5.

[10] Y. Chen, S. Zhu, Z. Fang, C. Liu, B. Zou, L. Qiu, Y. Wang, S. Chang, F. Jia, F. Qin, J. Fan, Y. Peng, C. Wang, Toward robust early detection of alzheimer’s disease via an integrated multimodal learning approach, in: *2025 IEEE International Conference on Acoustics, Speech and Signal Processing*, 2025, pp. 1–5.

[11] H. Zhou, F. Zhou, C. Zhao, Y. Xu, L. Luo, H. Chen, Multimodal data integration for precision oncology: Challenges and future directions, *arXiv preprint arXiv:2406.19611* (2024).

[12] I. Goodfellow, J. Pouget-Abadie, M. Mirza, B. Xu, D. Warde-Farley, S. Ozair, A. Courville, Y. Bengio, Generative adversarial networks, *Communications of the ACM* 63 (2020) 139–144.

[13] D. P. Kingma, M. Welling, Auto-Encoding variational bayes, *CoRR* abs/1312.6114 (2013).

[14] S. Bakas, M. Reyes, A. Jakab, S. Bauer, M. Rempfler, A. Crimi, R. T. Shinohara, C. Berger, S. M. Ha, M. Rozycski, et al., Identifying the best

machine learning algorithms for brain tumor segmentation, progression assessment, and overall survival prediction in the BRATS challenge, arXiv preprint arXiv:1811.02629 (2018).

- [15] M. C. de Verdier, R. Saluja, L. Gagnon, D. LaBella, U. Baid, N. H. Tahon, M. Foltyn-Dumitru, J. Zhang, M. Alafif, S. Baig, et al., The 2024 brain tumor segmentation (BraTS) challenge: Glioma segmentation on post-treatment MRI, arXiv preprint arXiv:2405.18368 (2024).
- [16] T. Karras, M. Aittala, J. Hellsten, S. Laine, J. Lehtinen, T. Aila, Training generative adversarial networks with limited data, *Advances in Neural Information Processing Systems* 33 (2020) 12104–12114.
- [17] H. Wang, C. Ma, J. Zhang, Y. Zhang, J. Avery, L. Hull, G. Carneiro, Learnable cross-modal knowledge distillation for multi-modal learning with missing modality, in: *International Conference on Medical Image Computing and Computer-Assisted Intervention*, 2023, pp. 216–226.
- [18] H. Wang, Y. Chen, C. Ma, J. Avery, L. Hull, G. Carneiro, Multi-modal learning with missing modality via shared-specific feature modelling, in: *Proceedings of the IEEE/CVF Conference on Computer Vision and Pattern Recognition*, 2023, pp. 15878–15887.
- [19] H. Ting, M. Liu, Multimodal Transformer of incomplete MRI data for brain tumor segmentation, *IEEE Journal of Biomedical and Health Informatics* 28 (2023) 89–99.
- [20] Z. Yu, X. Han, S. Zhang, J. Feng, T. Peng, X.-Y. Zhang, MouseGAN++: unsupervised disentanglement and contrastive representation for multiple MRI modalities synthesis and structural segmentation of mouse brain, *IEEE Transactions on Medical Imaging* 42 (2022) 1197–1209.
- [21] H. Yang, J. Sun, Z. Xu, Learning unified hyper-network for multi-modal MR image synthesis and tumor segmentation with missing modalities, *IEEE Transactions on Medical Imaging* 42 (2023) 3678–3689.
- [22] Z. Li, Y. Zhang, H. Li, Y. Chai, Y. Yang, Deformation-aware and reconstruction-driven multimodal representation learning for brain tumor segmentation with missing modalities, *Biomedical Signal Processing and Control* 91 (2024) 106012.

- [23] Q. Fan, H. Yuan, H. Zuo, R. Liu, G. Gao, Leveraging retrieval augment approach for multimodal emotion recognition under missing modalities, arXiv preprint arXiv:2410.02804 (2024).
- [24] C. Zhang, X. Chu, L. Ma, Y. Zhu, Y. Wang, J. Wang, J. Zhao, M3Care: Learning with missing modalities in multimodal healthcare data, in: Proceedings of the 28th ACM SIGKDD conference on knowledge discovery and data mining, 2022, pp. 2418–2428.
- [25] Y. Sun, Z. Liu, Q. Z. Sheng, D. Chu, J. Yu, H. Sun, Similar modality completion-based multimodal sentiment analysis under uncertain missing modalities, *Information Fusion* 110 (2024) 102454.
- [26] X. Li, J. Jin, Y. Zhou, Y. Zhang, P. Zhang, Y. Zhu, Z. Dou, From matching to generation: A survey on generative information retrieval, *ACM Transactions on Information Systems* 43 (2025) 1–62.
- [27] T. Wang, F. Li, L. Zhu, J. Li, Z. Zhang, H. T. Shen, Cross-Modal retrieval: A systematic review of methods and future directions, *Proceedings of the IEEE* 112 (2024) 1716–1754.
- [28] Y. Ding, X. Yu, Y. Yang, RFNet: Region-aware fusion network for incomplete multi-modal brain tumor segmentation, in: Proceedings of the IEEE/CVF International Conference on Computer Vision, 2021, pp. 3975–3984.
- [29] Y. Zhang, N. He, J. Yang, Y. Li, D. Wei, Y. Huang, Y. Zhang, Z. He, Y. Zheng, mmFormer: Multimodal medical transformer for incomplete multimodal learning of brain tumor segmentation, in: International Conference on Medical Image Computing and Computer-Assisted Intervention, 2022, pp. 107–117.
- [30] J. Shi, L. Yu, Q. Cheng, X. Yang, K.-T. Cheng, Z. Yan, MFTrans: Modality-masked fusion transformer for incomplete multi-modality brain tumor segmentation, *IEEE Journal of Biomedical and Health Informatics* 28 (2023) 379–390.
- [31] C. Chen, Q. Dou, Y. Jin, H. Chen, J. Qin, P.-A. Heng, Robust multi-modal brain tumor segmentation via feature disentanglement and gated fusion, in: International Conference on Medical Image Computing and Computer-Assisted Intervention, 2019, pp. 447–456.

- [32] S. Jeong, H. Cho, J. Kwon, H. Park, Region-of-interest attentive heteromodal variational encoder-decoder for segmentation with missing modalities, in: Proceedings of the Asian Conference on Computer Vision, 2022, pp. 3707–3723.
- [33] S. Zhu, Y. Chen, S. Jiang, W. Chen, C. Liu, Y. Wang, X. Chen, Y. Ke, F. Qin, C. Wang, et al., XLSTM-HVED: Cross-modal brain tumor segmentation and MRI reconstruction method using vision XLSTM and heteromodal variational encoder-decoder, in: International Symposium on Biomedical Imaging, 2025, pp. 1–5.
- [34] Y. Wang, Y. Zhang, Y. Liu, Z. Lin, J. Tian, C. Zhong, Z. Shi, J. Fan, Z. He, Acn: Adversarial co-training network for brain tumor segmentation with missing modalities, in: International Conference on Medical Image Computing and Computer-Assisted Intervention, 2021, pp. 410–420.
- [35] Z. Ning, S. Zhong, Q. Feng, W. Chen, Y. Zhang, SMU-Net: Saliency-guided morphology-aware U-Net for breast lesion segmentation in ultrasound image, *IEEE Transactions on Medical Imaging* 41 (2021) 476–490.
- [36] S. Zhu, Y. Chen, W. Chen, Y. Wang, C. Liu, S. Jiang, F. Qin, C. Wang, Bridging the gap in missing modalities: Leveraging knowledge distillation and style matching for brain tumor segmentation, *arXiv preprint arXiv:2507.22626* (2025).
- [37] D. Li, B. Yang, W. Zhan, X. He, Multi-category graph reasoning for multi-modal brain tumor segmentation, in: International Conference on Medical Image Computing and Computer-Assisted Intervention, 2024, pp. 445–455.
- [38] P. Veličković, G. Cucurull, A. Casanova, A. Romero, P. Liò, Y. Bengio, Graph attention networks, *International Conference on Learning Representations* (2018).
- [39] B. H. Menze, A. Jakab, S. Bauer, J. Kalpathy-Cramer, K. Farahani, J. Kirby, Y. Burren, N. Porz, J. Slotboom, R. Wiest, et al., The multimodal brain tumor image segmentation benchmark (BRATS), *IEEE Transactions on Medical Imaging* 34 (2014) 1993–2024.